RSC Advances

REVIEW

View Article Online
View Journal | View Issue

Cite this: *RSC Adv.*, 2026, **16**, 6562

^{17}O NMR spectroscopy in polyoxometalate chemistry: advances, challenges, and applications in structure and catalysis

Thompson Izuagie [a] and Daniel Lebbie[b]

^{17}O Nuclear Magnetic Resonance (NMR) spectroscopy has become an increasingly valuable technique for investigating the structure, dynamics, and reactivity of polyoxometalates (POMs), a diverse class of metal–oxygen clusters with broad applications in catalysis, energy storage, and materials science. The oxygen framework of POMs plays a very important role in dictating their physical and chemical properties, making direct probing of oxygen environments essential. However, the quadrupolar nature and low natural abundance (0.037%) of ^{17}O nuclei impose significant experimental challenges, including low sensitivity and broad line shapes. Recent methodological breakthroughs such as the development of ultra-high-field NMR instrumentation, the use of magic angle spinning (MAS) to minimize anisotropic broadening, and the implementation of dynamic nuclear polarisation (DNP) to boost signal intensity have greatly enhanced the resolution and feasibility of ^{17}O NMR studies. These advances now enable the differentiation of terminal, bridging, and internal oxygen sites, offering unique insights into structural isomerism, substitution effects, and protonation states in various POM archetypes including Lindqvist, Keggin, and Dawson structures. Beyond structural assignments, ^{17}O NMR has provided mechanistic understanding of catalytic processes by tracking oxygen participation in redox transformations and proton-coupled electron transfer. When integrated with computational approaches such as density functional theory (DFT) and artificial intelligence (AI), ^{17}O NMR delivers predictive power for interpreting chemical shifts, quadrupolar parameters, and dynamic behaviour. This review consolidates recent progress, highlights case studies, and underscores the emerging role of ^{17}O NMR as a cornerstone for advancing POM chemistry at the interface of structural science, catalysis, and theoretical modeling.

Received 1st November 2025
Accepted 19th January 2026

DOI: 10.1039/d5ra08401f

rsc.li/rsc-advances

[a]*Department of Chemistry, National Open University of Nigeria, University Village, Plot 91, Cadastral Zone, Jabi, Abuja 900107, Nigeria. E-mail: Tizuagie@noun.edu.ng; tomyi2012@yahoo.com*

[b]*37 Peacock Drive Highfields, Caldecote, Cambridge, CB23 7FE, UK*

Thompson Izuagie

Thompson Izuagie is a Reader (Associate Professor) of Chemistry at the National Open University of Nigeria (NOUN), Abuja. He received his PhD in Chemistry from Newcastle University, UK, in 2017 under the supervision of R. John Errington, following earlier BSc and MSc degrees from Usmanu Danfodiyo University, Sokoto, Nigeria. His research interests span inorganic and sustainable chemistry, with particular emphasis on polyoxometalates, multinuclear NMR spectroscopy, and bio-derived hybrid materials for water purification and environmental applications. He has published widely and is actively involved in chemical education, outreach, and professional service.

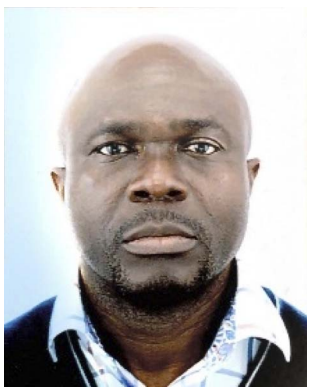

Daniel Lebbie

Daniel Lebbie is a chemist specialising in the synthesis, structure, and reactivity of polyoxometalates. He obtained his PhD in Chemistry from Newcastle University, UK, in 2020 under the supervision of R. John Errington, where his research focused on non-aqueous synthesis and reactivity of early transition-metal polyoxoanions, with particular emphasis on Lindqvist-type polyoxometalates. He previously earned an MPhil in Chemistry from Newcastle University, investigating tin- and titanium-substituted Lindqvist systems, and a BSc (Hons) in Chemistry from Fourah Bay College, University of Sierra Leone. His research interests include polyoxometalate chemistry, non-aqueous reactivity, and structure–reactivity relationships.

1 Introduction

Polyoxometalates (POMs) are discrete metal–oxygen clusters, typically composed of early-transition metals (*e.g.* V, Mo, W, Nb, Ta) in high oxidation states, linked by oxide bridges to form robust molecular architectures.[1,2] Their tunable redox properties, structural modularity, and rich acid–base behaviour have made them versatile agents in catalysis (oxidation, acid, photoredox), energy conversion and storage (electrocatalysis, charge storage), and advanced materials design (molecular electronics, hybrid frameworks). Recent reviews have emphasised the rise of POM-based materials, especially in electrocatalysis (water splitting, CO_2 reduction, nitrogen reduction) and energy storage devices (supercapacitors, batteries).[2–4]

In catalysis, POMs can mediate multi-electron redox processes with high stability, serving as homogeneous or immobilized catalysts; hybrid POM–metal–organic framework or POM–carbon composites further enhance performance through synergistic effects.[5–7] In materials science, POMs have been integrated into conductive matrices, grafted onto surfaces, and used as building blocks in nanoarchitectures due to their structural versatility (*e.g.* covalent anchoring to oxides).[8,9] Thus, the molecular precision of POMs and their potential for scalable functionality make them central to current efforts in sustainable catalysis and energy materials.

The oxygen atoms in POM frameworks play more than just scaffolding roles. They mediate the geometry, electronic structure, redox pathways, protonation equilibria, and catalytic reactivity of POMs.[10] Different oxygen types: terminal (M=O), bridging (μ_2–O, μ_3–O), interior oxo, or protonated species (as described in Fig. 1), exhibit distinct bonding, electron density, and reactivity. The differentiation of these sites is crucial to understand isomerism, heteroatom substitution, proton-coupled electron transfer, and dynamic behaviours in POMs. For example, protonation often happens at bridging O sites, altering local electron density and reactivity; discerning which oxygen is protonated under different pH is a key mechanistic question.

Because many other spectroscopic probes (*e.g.* vibrational, X-ray, IR, Raman) identify overall M–O bonding or collective modes, they often mix-up multiple oxygen sites or lack the site-specific resolution needed to assign subtle structural or reactive changes. Hence, a direct, site-sensitive probe of oxygen is highly necessary to reveal structural undertones that govern reactivity.

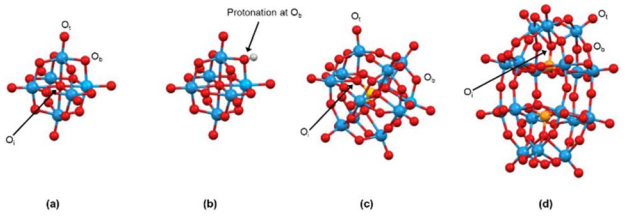

Fig. 1 Ball-and-stick models of archetypal POMs illustrating terminal (O_t), bridging (O_b), and internal (O_i) sites that define characteristic ^{17}O resonances. (a) Lindqvist-type $[M_6O_{19}]^{n-}$ (b) protonated-Lindqvist-type $H[M_6O_{19}]^{(n-1)-}$. (c) Keggin-type $[XM_{12}O_{40}]^{n-}$ and (d) Dawson-type $[X_2M_{18}O_{62}]^{n-}$ structure.

^{17}O Nuclear Magnetic Resonance (NMR) offers a unique advantage: it probes oxygen nuclei directly, delivering site-specific chemical shifts, quadrupolar coupling parameters, and line shapes that reflect local electronic environments. Unlike indirect probes, ^{17}O NMR can discriminate between terminal, bridging, and internal oxygens and detect protonation or heteroatom substitution effects. Early foundational works and subsequent studies established that ^{17}O NMR spectra of oxometalates are sensitive to oxidation state, coordination, and metal–oxygen bonding interactions.[11–14]

However, ^{17}O NMR in POMs faces two intrinsic challenges. Firstly, ^{17}O is a spin-5/2 quadrupolar nucleus, subject to quadrupole broadening; and secondly its natural abundance is extremely low (~0.037%), leading to weak sensitivity. Overcoming these obstacles has required advances in high-field NMR, magic angle spinning (MAS), high-resolution pulse sequences, and recent enhancements such as dynamic nuclear polarisation (DNP). In addition, coupling ^{17}O NMR with computational methods (especially density functional theory, DFT) enables predictive modelling of shifts and quadrupolar parameters, bridging experiment and theory. For example, theoretical studies have shown that DFT (especially with hybrid functionals) can predict ^{17}O chemical shifts in POMs with reasonable accuracy, and probe the impact of protonation or metal substitution.[13,15]

Several reviews have discussed ^{17}O NMR in metal oxides and clusters more generally[16–18] or discrete metal-oxide clusters,[14,19,20] but a focused exposition on its role in POM chemistry is timely given recent advances and applications. In light of these developments, this review aims to provide a comprehensive, up-to-date synthesis of the principles, breakthroughs, and applications of ^{17}O NMR spectroscopy as applied to polyoxometalate chemistry. The review will (i) present the fundamentals of ^{17}O NMR in quadrupolar systems; (ii) survey methodological advances that enhance sensitivity and resolution (*e.g.* high-field, MAS, DNP, optimised pulse sequences); (iii) highlight representative case studies where ^{17}O NMR has elucidated oxygen environments, structural assignment, protonation equilibria, and catalytic mechanisms in POMs; (iv) discuss the integration of ^{17}O NMR with computational modelling (especially DFT) and Artificial Intelligence (AI) and how these synergies enable predictive insights; and (v) outline current challenges, open questions, and future opportunities for applying ^{17}O NMR to novel POM systems in catalysis, energy, and materials research. Through this review, we seek to establish ^{17}O NMR not just as a complementary tool but as a central method in the molecular-level study of POM structure–function relationships. To facilitate interpretation of ^{17}O NMR data and the parameters discussed throughout this review, a glossary of terms and key spectroscopic constants is provided below (Table 1) while other terms not captured in the table are explained in the abbreviations section.

2 Principles of ^{17}O NMR spectroscopy

^{17}O is a low-γ (gyromagnetic ratio), quadrupolar nucleus (spin $I = {}^5/_2$) with a natural abundance of ~0.037%, which makes it

Table 1 Key terms and parameters in ^{17}O NMR of POMs

Symbol/term	Definition and physical meaning
δ (Chemical shift)	The displacement of the resonance frequency of a nucleus from a reference compound, expressed in ppm: $\delta = \frac{(\nu - \nu_{ref})}{\nu_{ref}} \times 10^6$. For ^{17}O, δ reflects local electronic shielding ($\delta(^{17}O)$) and is sensitive to M–O bond type, protonation, and substitution
δ_{iso} (Isotropic shift)	The orientation-independent average of the principal components of the chemical shift tensor: $\delta_{iso} = \frac{1}{3}(\delta_{11} + \delta_{22} + \delta_{33})$. It is used for comparing sites across POM families (O_t, O_b/O_c, O_i)
C_Q (Quadrupolar coupling constant)	A measure of the interaction between the nuclear quadrupole moment (Q) and the principal component (eq) of the local electric-field gradient (EFG): $C_Q = \frac{e^2qQ}{h}$ (where e = elementary charge, q = principal component of EFG tensor, h = Planck's constant). It quantifies the magnitude of quadrupolar broadening in ^{17}O ($I = 5/2$)
η (Asymmetry parameter)	Describes deviation of the EFG from axial symmetry: $\eta = \frac{V_{xx} - V_{yy}}{V_{zz}} (0 \le \eta \le 1)$ $\eta = 0$ indicates perfect axial symmetry; higher η values indicate local distortion
EFG (Electric-field gradient)	Tensor describing the spatial variation of the electric field at the nucleus, arising from local electron distribution and bonding asymmetry. It determines C_Q and η
σ (Magnetic shielding tensor)	Second-rank tensor describing how local electron circulation shields the nucleus from the external magnetic field. The observable shift is $\delta = \sigma_{ref} - \sigma$
^{17}O natural abundance	The fractional abundance of ^{17}O is 0.037%, making signal enhancement or isotopic enrichment essential for solid-state studies
γ (Gyromagnetic ratio)	This connects a nucleus's magnetic moment (μ) to its angular momentum (I). It determines the strength of its magnetic interaction, its resonance frequency, and its NMR sensitivity
O_t/O_b/O_c/O_i	O_t = terminal oxygen (M=O), O_b/O_c = bridging oxygen between metals (μ_2–O), O_i = internal or encapsulated oxygen (μ_3–μ_6–O). Each site type shows characteristic δ and C_Q ranges
μ-O notation	Greek μ indicates the number of metal centers an oxygen atom bridges: μ_2 (two metals), μ_3 (three), μ_6 (six) *etc.*
MAS (Magic-angle spinning)	High-speed rotation of the sample (typically 10–160 kHz) at 54.74° relative to B_0 to average out anisotropic interactions, sharpening lines in solids
MQMAS (Multiple-quantum MAS)	2D NMR method that correlates multiple- and single-quantum coherences, separating isotropic and quadrupolar effects to enhance resolution for $I > \frac{1}{2}$ nuclei such as ^{17}O
STMAS (Satellite-transition MAS)	Alternative 2D method using satellite transitions to obtain high-resolution isotropic spectra of quadrupolar nuclei
HETCOR (Heteronuclear correlation)	Two-dimensional experiment correlating chemical shifts of different nuclei (*e.g.*, ^{1}H–^{17}O or ^{17}O–^{183}W), providing connectivity and hydrogen-bonding information
DNP (Dynamic nuclear polarisation)	Sensitivity-enhancement technique where microwave irradiation transfers spin polarisation from unpaired electrons to nearby nuclei, increasing signal by 10^2–10^3 times
DFT (Density functional theory)	Quantum mechanical computational framework for electronic structure calculations. It is used to predict NMR shielding (σ) and EFG tensors for structural assignment
GIPAW (Gauge-including projector augmented-wave)	Plane-wave DFT implementation enabling accurate calculation of chemical shifts and quadrupolar parameters in periodic solids
OAT (Oxygen-atom transfer)	A redox process where an oxygen atom is transferred between donor and acceptor species (*e.g.*, POM + substrate → reduced POM + oxidised product)
PCET (Proton-coupled electron transfer)	A reaction mechanism involving the simultaneous transfer of protons and electrons – central to POM-mediated redox catalysis
Operando ^{17}O NMR	Real-time monitoring of ^{17}O environments during active catalytic or exchange processes under realistic reaction conditions

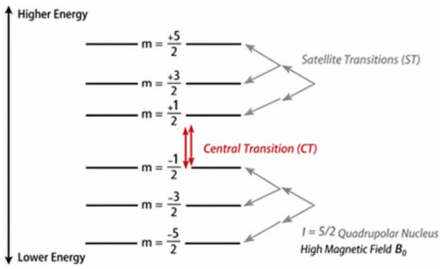

Fig. 2 Energy-level diagram for a half-integer quadrupolar nucleus ($I = 5/2$), illustrating the central transition ($m = +\frac{1}{2} \leftrightarrow -\frac{1}{2}$), which is least affected by first-order quadrupolar interactions and is therefore the dominant feature observed in solid-state ^{17}O MAS NMR, and the satellite transitions ($\pm 3/2 \leftrightarrow \pm 1/2$, $\pm 5/2 \leftrightarrow \pm 3/2$), which are broadened by quadrupolar effects. Diagram is schematic and not to scale; quadrupolar interactions modify level spacing and transition frequencies.

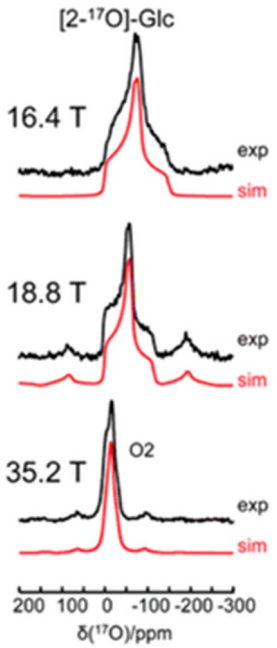

Fig. 3 Comparison of solid-state ^{17}O MAS NMR spectra of [2-^{17}O] α-D-glucose acquired at increasing magnetic field strengths (16.4, 18.8, and 35.2 T), illustrating the progressive reduction of second-order quadrupolar broadening of the central transition and the corresponding improvement in spectral resolution and site discrimination at ultrahigh fields. Adapted from ref. 33. Copyright 2022, Royal Society of Chemistry.

intrinsically insensitive in both solution and solid-state NMR experiments. In isotropic solution, rapid molecular tumbling averages first-order anisotropic interactions; however, second-order quadrupolar interactions can still contribute significantly to line broadening and transverse relaxation, particularly for larger molecules or in slow-motion regimes. Theoretical treatments of nuclear quadrupole relaxation show that quadrupolar contributions to central-transition linewidths depend strongly on molecular correlation time and magnetic field strength, with second-order and cross-correlated relaxation mechanisms dominating for half-integer nuclei such as ^{17}O.[21,22] In contrast, in the solid state where rapid isotropic tumbling is absent, the residual second-order quadrupolar interaction between the nuclear electric quadrupole moment and the local electric field gradient (EFG) is a dominant determinant of central transition line shapes even under magic-angle spinning (MAS).[17,23,24] This second-order broadening depends on the quadrupolar coupling constant and the asymmetry parameter and is typically treated using perturbation theory for half-integer spins in solids, giving rise to characteristic broadened powder patterns whose analysis yields site-specific quadrupolar parameters. Comprehensive theoretical treatments of quadrupolar interactions including their quantum-mechanical origin, line-shape formalisms, and magnetic-field dependence are provided in authoritative solid-state NMR monographs by Duer and by MacKenzie and Smith, which remain foundational references for understanding quadrupolar effects in inorganic materials.[23,24] In addition, several modern review articles provide detailed discussions of experimental manifestations of quadrupolar broadening and its mitigation using techniques such as MAS, MQMAS, and STMAS.[19,25–28]

Despite these challenges, ^{17}O NMR is uniquely powerful because oxygen sites in oxometalates and related materials span an exceptionally wide chemical-shift range (approximately −100 to >1200 ppm) and exhibit site-specific quadrupolar parameters *i.e.* quadrupolar coupling constant (C_Q) and asymmetry parameter (η) that encode local symmetry, bonding, and protonation.[13] When sensitivity limitations are overcome, these parameters enable differentiation of terminal, bridging, and internal oxygen environments, detection of subtle coordination changes, and insight into hydrogen bonding and proton-coupled electron-transfer processes.

For materials and cluster chemists, the most practical takeaway is the favourable field scaling of second-order quadrupolar broadening. For a half-integer quadrupolar nucleus ($I \geq 3/2$), such as ^{17}O with ($I = 5/2$) the second-order quadrupolar shift of the central transition ($m = \frac{1}{2} \leftrightarrow -\frac{1}{2}$), illustrated in Fig. 2, in the high-field approximation is:

$$\Delta\nu_Q^{(2)} = \frac{{C_Q}^2}{\nu_0} \times \frac{\left(1 + \frac{\eta^2}{3}\right) f(I)}{40}$$

where

$$f(I) = \frac{I(I+1) - \frac{3}{4}}{I^2(2I-1)^2}$$

and

$$\text{Quadrupolar coupling constant(Hz)}, C_Q = \frac{e^2 q Q}{h}$$

$$\text{Asymmetry parameter of the EFG}, \eta = \frac{V_{xx} - V_{yy}}{V_{zz}}$$

$$(0 \leq \eta \leq 1)$$

$$\text{Larmor frequency(Hz)}, \nu_0 = \frac{\gamma B_0}{2\pi}$$

B_0 = static magnetic-field strength (T) and

eqQ = product of electric-field-gradient principal component and nuclear quadrupole moment

$$\text{Since } \nu_0 \propto B_0,$$

$$\Delta\nu_Q^{(2)} \propto \frac{{C_Q}^2}{B_0}$$

These expressions arise from second-order perturbation treatments of the quadrupolar Hamiltonian for half-integer spins in the high-field limit and have been derived rigorously in the foundational works of Abragam, Slichter, and later formalised for magic-angle spinning by Vega, Amoureux, and co-workers.[17,22,29–31] Consequently, second-order quadrupolar broadening decreases inversely with the static magnetic field strength, leading to narrower and better-resolved spectra at higher B_0 (*e.g.*, ≥28 T), as illustrated by the representative multi-field MAS spectra in Fig. 3. This comparison highlights the central role of ultrahigh magnetic fields in mitigating quadrupolar broadening, which underpins the major impact of ultrahigh-field NMR on quadrupolar nuclei and provides a key rationale for employing ultrahigh-field MAS NMR in ^{17}O studies of polyoxometalates and related systems. In practice, increasing the field from conventional strengths (up to ~9.4 T) to the ultrahigh-field regime (20–35.2 T) enables markedly cleaner, site-selective spectral assignments, an effect demonstrated in recent ^{17}O NMR studies using 17.6–35.2 T magnets.[32]

2.1 Experimental challenges

^{17}O NMR studies are confronted by two major experimental challenges: isotopic enrichment and sensitivity.

2.1.1 Isotopic enrichment. Because the natural-abundance of ^{17}O is so low, most experiments require enrichment to reach practical acquisition times. Two general strategies are used.

2.1.1.1 $H_2{}^{17}O$ exchange/enrichment. This method is employed at the molecule or material level (*via* hydrothermal synthesis, post-synthetic exchange, or mechanochemical routes[34,35]) to incorporate ^{17}O into targeted oxo sites. This is particularly common for oxometalates and microporous/inorganic frameworks, where exchange with enriched water labels terminal and bridging oxygens to varying extents. Solution studies of POM speciation and many solid-state applications document $H_2{}^{17}O$ as a straightforward, flexible label source.[10,36–44] To illustrate the practicality of $H_2{}^{17}O$ labeling at the material level, Fig. 4A presents time-resolved ^{17}O MAS and MQMAS (isotropic) projections for a simple room-temperature slurry of H-mordenite (H-MOR) with liquid $H_2{}^{17}O$. The spectra show rapid framework incorporation of ^{17}O that is readily tracked as a function of hydration time, with early signals emphasising Si–O–Al linkages and broader framework enrichment (including Si–O–Si) emerging at longer times, emphasising the site-dependent access and exchange expected for oxo networks in zeolites and oxometalate clusters. This bench-top approach requires no specialized apparatus, avoids high-temperature side effects (*e.g.*, dealumination), yet yields enrichment levels comparable in magnitude to gas-phase routes, making it a flexible, cost-effective pathway for labeling targeted oxo sites. The room temperature enrichment method with $H_2{}^{17}O$ in acetonitrile where enriched solvent can be reused has been demonstrated for the $[NaPW_{11}O_{39}]^{6-}$.[36,37] These data support the central point of this review that: $H_2{}^{17}O$ serves as a straightforward, versatile label source that differentially tags terminal/bridging oxygens (or framework linkages) and enables both mechanistic and site-selective studies by ^{17}O NMR. To further benchmark room-temperature $H_2{}^{17}O$ slurry exchange against a conventional high-temperature post-synthetic route, Fig. 4B shows ^{17}O MAS and MQMAS spectra for H-mordenite (H-MOR) enriched post-synthesis by gas-phase $^{17}O_2$. In this protocol, exposure at 600 °C for 12 h gives extensive framework labeling and a site distribution that is broadly consistent with more uniform enrichment expected under high-temperature conditions, in contrast to the time-dependent, initially selective uptake seen in slurries. Notably, the MQMAS comparison indicates a slightly shifted/broader Si–^{17}O–Si response for the gas-enriched solid, implying that some Si–O–Si sites label less readily under room-temperature slurry conditions. Despite mechanistic differences, the overall enrichment levels are of

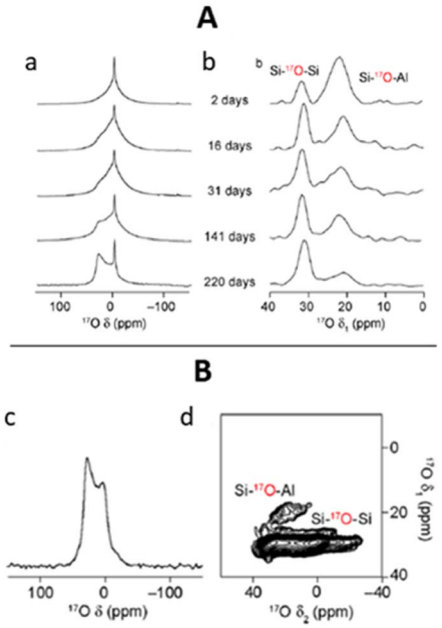

Fig. 4 ^{17}O (14.1 T) (A) (a) MAS and (b) isotropic projections of MQMAS NMR spectra of a 50 μL/50 mg slurry of H-MOR/$H_2{}^{17}O$(l) after varying times. Spectra are shown normalized and (B) (c) MAS and (d) MQMAS NMR spectra of H-MOR enriched postsynthesis by exchange with $^{17}O_2$(g). The figures and the caption are adapted with permission from ref. 43. Copyright 2020, American Chemical Society.

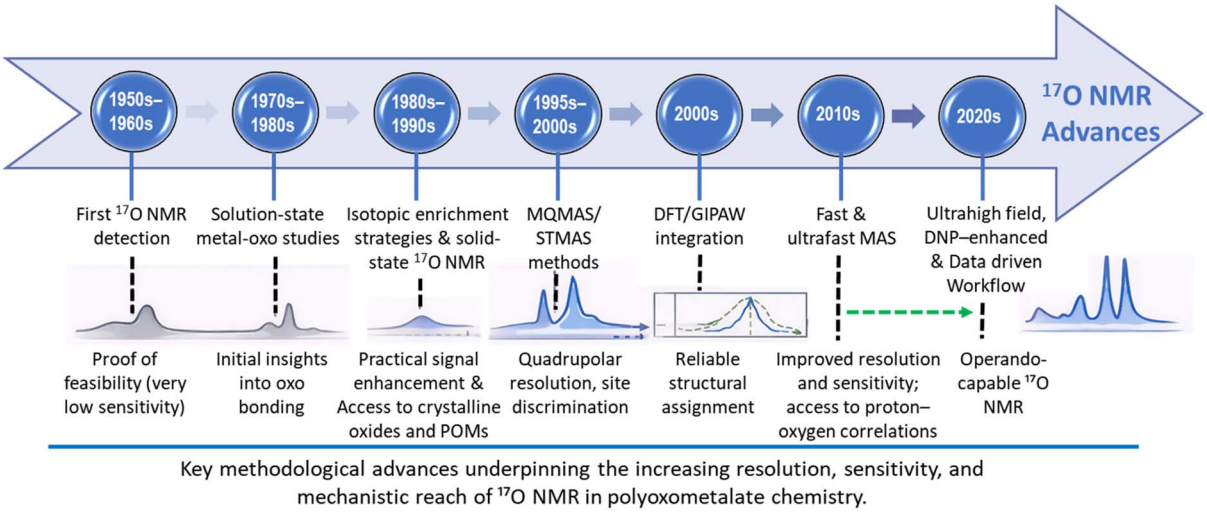

Fig. 5 Timeline of key methodological advances in ^{17}O NMR spectroscopy and their impact on polyoxometalate (POM) studies. From the first detection of ^{17}O NMR signals in the 1950s–1960s,[18,56] through the introduction of isotopic enrichment, magic-angle spinning (MAS), and high-resolution quadrupolar methods (MQMAS/STMAS) in the 1990s–2000s,[11,57–61] to the integration of first-principles calculations, fast MAS, ultrahigh magnetic fields, and dynamic nuclear polarisation (DNP) in the 2010s–2020s,[62–65] each methodological breakthrough has progressively improved spectral sensitivity, resolution, and site discrimination. Representative schematic spectra illustrate how these advances have expanded the structural and mechanistic reach of ^{17}O NMR for POM chemistry.

similar order for both approaches (with the slurry giving approximately 2–3 times more ^{17}O signal under the reported conditions), underscoring that either route can deliver analytically useful labeling while trading off energy cost and potential framework perturbation at high temperature.

2.1.1.2 Synthetic incorporation. This protocol employs ^{17}O-labeled precursors or solid–gas exchange and involves modern, cost-efficient methods (including mechanochemical saponification or milling) that have drastically reduced ^{17}O-water consumption while achieving 10–40% enrichment in targeted functional groups. The methods are generally applicable beyond biomolecules to inorganic solids and surfaces. Broader studies now catalogue ^{17}O-labeling strategies for bulk and surface oxygens, including in metal oxides relevant to energy materials.[20,45,46]

2.1.2 Sensitivity and line-width. Even when enriched, ^{17}O spectra can be broad and weak. The primary tools available to spectroscopists are: (i) higher B_0, which narrows second-order broadening and improves Boltzmann polarisation; (ii) faster MAS and advanced excitation/detection schemes (*e.g.*, MQMAS, STMAS, heteronuclear correlation, proton-detected methods) to separate isotropic and anisotropic contributions; and (iii) hyperpolarisation (dynamic nuclear polarisation, DNP) to boost signal intensities by orders of magnitude. These approaches, particularly in combination, have enabled routine observation of multiple inequivalent oxygen sites, even in complex or disordered solids, and under favourable conditions at or near natural abundance.[20,47–55]

2.2 Methodological advances in ^{17}O NMR

The ^{17}O NMR technique has undergone substantial methodological advances aimed at overcoming its inherent challenges of low natural abundance and strong quadrupolar broadening. Key developments include the introduction of high-field NMR instrumentation, magic-angle spinning (MAS), and dynamic nuclear polarisation (DNP). As summarised in Fig. 5, these advances have progressively transformed ^{17}O NMR from a niche, low-sensitivity probe into a high-resolution and increasingly operando-capable technique for oxygen chemistry. The timeline traces early limitations through the advent of MAS and multiple-quantum methods (MQMAS/STMAS), which enabled site-specific resolution, followed by the integration of GIPAW-DFT calculations that established quantitative structure-spectra correlations. More recent innovations such as ultrahigh magnetic fields (≥28 T), fast and ultrafast MAS (≥40–100 kHz), ^{1}H-detected correlation experiments, and DNP-based sensitivity enhancement, have further expanded the scope of ^{17}O NMR. Together with emerging AI-assisted computational workflows, these developments now allow precise, time-resolved interrogation of oxygen coordination, exchange, and redox dynamics in complex materials, including polyoxometalates.

2.2.1 High-field NMR. Gigahertz-class spectrometers, *e.g.* 28.2 T (1.2 GHz) HTS/LTS hybrid systems, ~30.5 T (1.3 GHz) next-gen HTS platforms, and 35.2 T (1.5 GHz) series-connected-hybrid magnets at the NHMFL, now available at national laboratories and selected facilities, provide transformative gains for ^{17}O.[66] Because second-order quadrupolar effects scale inversely with ν_0, spectra recorded at 28–35 T often resolve overlapping oxygen environments that are inseparable at 9.4–14.1 T. Multi-field data collections (*e.g.*, 17.6–35.2 T) further allow disentangling chemical-shift and quadrupolar contributions *via* field-dependent line-shape analysis, which is especially powerful for assigning oxygen sites in complex oxides, zeolites, and molecular oxo clusters.[32,67–71] Recent work demonstrates

residue-specific ^{17}O assignments in solids by combining ultra-high field with fast MAS and indirect ^{1}H detection – an approach whose principles readily translate to inorganic materials and polyoxometalates.[50] Reviews of ultrahigh-field hardware (*e.g.*, hybrid HTS/LTS outsert–insert designs and series-connected-hybrid magnets with enhanced field stability) highlight the rapid move toward routine >20 T experiments.[72–76]

2.2.2 MAS techniques and correlation methods. MAS suppresses orientation-dependent interactions, sharpening ^{17}O lines and enabling high-resolution 1D spectra.[25] For quadrupolar nuclei, however, residual second-order quadrupolar broadening persists under MAS. Nevertheless, MAS provides partial averaging and modest narrowing of the central transition relative to static spectra, even though complete removal of second-order effects is not achieved. Consequently, multiple-quantum MAS (MQMAS) and satellite-transition MAS (STMAS) experiments are employed to generate isotropic-like projections from which clean chemical shifts and quadrupolar parameters (C_Q, η) are obtained.[60,61] At high fields and fast MAS, 2D ^{17}O correlation experiments such as ^{17}O–^{17}O, ^{1}H–^{17}O, and ^{13}C–^{17}O using REAPDOR/REDOR-style recoupling or TEDOR variants; and HETCOR with indirect ^{1}H detection have become routine, improving sensitivity and enabling through-space connectivity measurements.[32,77] These advances have transformed ^{17}O into standard practice in solid-state studies of materials and molecular solids culminating in residue-specific ^{17}O assignments using multidimensional indirectly detected methods at ultrahigh field and fast MAS.[50,78,79]

A particularly impactful development is proton-detected ^{1}H → ^{17}O spectroscopy where polarisation is transferred from abundant protons and detection is performed on ^{1}H, delivering large sensitivity gains while preserving ^{17}O site specificity. Field-dependent parameters up to 35.2 T further disentangle quadrupolar and chemical-shift effects, yielding robust C_Q and δ_{iso} values.[32] Fig. 6 illustrates this contemporary ^{17}O method and demonstrates that MAS narrows lines while MQMAS removes residual second-order broadening to give isotropic-like ^{17}O projections (for δ_{iso}, C_Q and η). The figure also shows that complementary ^{1}H{^{17}O} HMQC maps at fast MAS boost sensitivity while providing site-specific ^{1}H ↔ ^{17}O correlations that link hydroxyl protons to resolved framework oxygens. Together, these elements explain why ^{17}O NMR is now a reliable, information-rich probe across diverse solid systems.

2.2.3 Dynamic nuclear polarisation (DNP). DNP, a technique that involves microwave-driven transfer of electron spin polarisation to nuclei, has revolutionized ^{17}O sensitivity. Early demonstrations showed that natural-abundance ^{17}O spectra of inorganic hydroxides, oxides and metal organic frameworks could be recorded in minutes under MAS DNP at ~18.8 T, where conventional experiments would be prohibitively long.[51,65,80] Subsequent studies refined radicals, pulse sequences, and cross-polarisation pathways (CE/OE mechanisms), extending DNP-^{17}O to surfaces, hydrates, and heterogeneous catalysts.[47,81–83] Contemporary reports position DNP as a general solution for low-γ, low-abundance nuclei in solids. Practically, it enables ^{17}O site observation in challenging systems (*e.g.*, thin surface layers, dilute ^{17}O environments, or poorly crystalline phases) and complements high-field/fast-MAS hardware advances.[47,52–55,80,83–86]

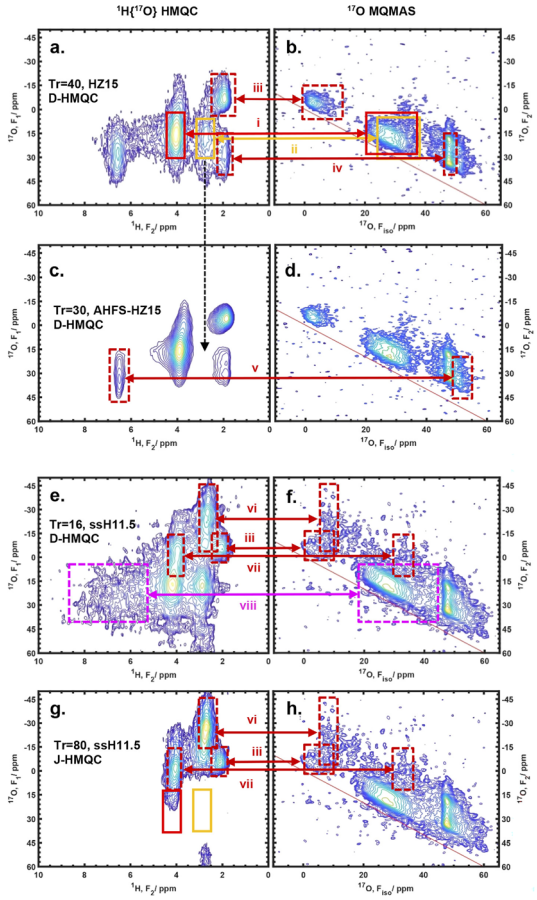

Fig. 6 Correlated 2D ^{1}H{^{17}O} D-HMQC (left column) and ^{17}O MQMAS (right column) correlation spectra for dry HZSM-5 zeolites acquired at 19.6 T and with 16 kHz MAS. (a and b) Si/Al = 15; (c and d) same as (a and b) after AHFS washing; (e and f) Si/Al = 11.5 after steaming; (g and h) same as (e and f) but with J-HMQC instead of D-HMQC. The figure and the caption are reprinted with permission from ref. 42. Copyright 2022, American Chemical Society.

2.3 Practical considerations and emerging best practices

Generally, efficient utilisation of ^{17}O NMR technique in POM studies would necessitate some emerging trends. Firstly, in designing samples for inorganic clusters and oxometalates, selective incorporation of $H_2{}^{17}O$ during synthesis or post-synthetic exchange can bias labelling toward terminal M=O or bridging μ–O sites, aiding assignments when combined with DFT predictions of δ_{iso} and EFG tensors. Multi-field analysis (*e.g.* 14.1/21.1/28–35 T), is recommended to validate extracted C_Q and η and to separate overlapping contributions. Also, fast MAS (≥40–60 kHz) and indirect ^{1}H detection maximize sensitivity for hydrated frameworks and hybrid solids. DNP becomes decisive when enrichment is limited, when sites are dilute, or for surface-selective probes. Finally, computational spectroscopy (GIPAW-DFT for periodic solids; hybrid functionals for clusters) is increasingly standard for correlating measured ^{17}O

parameters with local bonding geometries and protonation states. Modern reviews of ^{17}O in microporous/inorganic materials and of general solid-state methods provide practical roadmaps for experiment design.[20,49] Section 2.5 gives a summary of the practical implications of these advances.

2.4 How ^{17}O NMR compares with other techniques

To appreciate the central role of ^{17}O in modern structural and reactivity analysis, it is useful to consider it alongside complementary techniques such as XRD, IR/Raman, electron microscopy (SEM/TEM), XAS, and multinuclear NMR (^{183}W, ^{51}V, ^{27}Al), which are commonly applied to metal–oxide clusters chemistry. As noted earlier, ^{17}O solid-state NMR (ssNMR) directly probes the oxygen sublattice, resolving terminal M=O, μ-bridging, and interior O sites and reporting local symmetry and bonding through δ_{iso}, C_Q, and η. At ultrahigh fields (28–35.2 T) with fast MAS, overlapping oxygen environments can be deconvoluted and quadrupolar effects separated from chemical shift, enabling confident, site-specific assignments in framework oxides and POMs.[26,74,77] A concise comparison of ^{17}O ssNMR with these other methods is discussed below while Table 2 provides a summary of the best scenario to applied each technique.

2.4.1 Diffraction (single-crystal/powder XRD; total scattering/PDF). Diffraction yields precise average structures and long-range order but can be insensitive to hydrogen positions, mixed occupancies, local disorder, or subtle oxygen heterogeneity. In contrast, ^{17}O ssNMR is oxygen-centric and locally selective, revealing distinct O sites even in disordered or multiphase specimens; together, NMR and diffraction provide a complete picture (local *vs.* average).[26,87]

2.4.2 Vibrational spectroscopy (IR/Raman). IR/Raman are rapid, *operando*-friendly probes of functional groups (*e.g.*, V=O *vs.* M–O–M) and reaction progress, including under mechanochemical conditions. However, band congestion/mode coupling can obscure which specific O site changes. ^{17}O ssNMR attributes spectral changes to identified O positions (O_t *vs.* O_b/O_c) and quantifies electronic asymmetry *via* quadrupolar parameters; in practice, Raman/IR plus ^{17}O NMR offers complementary temporal resolution and site specificity.[87]

2.4.3 X-ray absorption spectroscopy (XANES/EXAFS). XAS excels at element-specific oxidation state and first-shell coordination under realistic conditions and is a mainstay of *in situ*/*operando* catalysis. It averages over oxygen neighbours to the selected metal and generally cannot distinguish individual O sites. ^{17}O ssNMR inverts the perspective by providing oxygen-site resolution. So, combining XAS (metal-centric) with ^{17}O NMR (oxygen-centric) is powerful for tracking lattice O *versus* peroxo/hydroxyl or surface O species.[88,89]

2.4.4 Electron microscopy (TEM/STEM/EDS/EELS). Microscopy provides real-space morphology, defect, and interface information at nanometer–Å scales, but direct speciation of oxygen electronic states remains challenging. ^{17}O ssNMR is bulk-representative and chemically specific to oxygen; pairing microscopy (where are features?) with ^{17}O NMR (what is the oxygen chemistry there?) is effective for supported or hybrid POM materials.

2.4.5 Other NMR nuclei and multinuclear strategies. Metal-center NMR (*e.g.*, ^{51}V, ^{27}Al) and $^{1}H/^{13}C$ report on cation environments, proton networks, and organics. ^{17}O answers "which oxygen is doing what?" Multinuclear correlation (*e.g.*, $^{17}O \leftrightarrow {}^{51}V/{}^{27}Al/{}^{11}B$) and DFT/GIPAW enable unambiguous oxygen-site assignment and mechanism mapping (*e.g.*, CO_2 adduct speciation in porous hosts).[26,77,90]

2.4.6 *Operando* and reactivity. Vibrational spectroscopies and XAS currently offer the broadest temperature/pressure windows and easiest *operando* deployment. ^{17}O ssNMR *operando* studies are increasingly tractable *via* high-field probes, rapid acquisition, robust liquid/gas-delivery MAS cells, and tailored pulse sequences. Method roadmaps now outline practical *operando* NMR workflows that POM/oxide studies can adopt, with ^{17}O being especially valuable where identity and dynamics of specific O species (lattice *vs.* peroxo *vs.* hydroxyl) control mechanism.[89,91]

Table 2 When to use what: complementary techniques for probing structure and reactivity in metal–oxide clusters (*e.g.*, POMs)

Technique	Best-use scenarios	Ref.
^{17}O solid-state NMR	When oxygen-site specificity, protonation mapping, or O-exchange kinetics control mechanism	26, 74, 77 and 90
Diffraction (SCXRD/PXRD/PDF)	Establishing crystal/phase models and average framework before local probes	26 and 87
Vibrational spectroscopy (IR/Raman)	Rapid screening of reactions/intermediates; follow bond making/breaking *in situ*	87
X-ray absorption (XANES/EXAFS; scattering)	*In situ*/*operando* redox and coordination mapping around metals; complements O-centric NMR	88 and 89
Electron microscopy (TEM/STEM/EELS)	Correlating particle size/defects/support interfaces with oxygen chemistry seen by ^{17}O NMR	88 and 89
Other NMR nuclei (^{1}H, ^{13}C, ^{27}Al, ^{51}V, *etc.*)	Multinuclear correlation (*e.g.*, $^{17}O \leftrightarrow {}^{51}V/{}^{27}Al/{}^{13}C$) to complete assignments and validate mechanisms	26, 74, 77 and 90

Despite low natural abundance and quadrupolar broadening, ^{17}O NMR offers an exceptionally site-specific view of oxygen chemistry, discriminating terminal, bridging, and interior oxo sites. Its spectral resolution improves markedly with increasing field strength; accordingly, ultrahigh-field (≥28 T) MAS combined with advanced multiple-quantum/correlation experiments has elevated ^{17}O NMR from a low-sensitivity niche to a robust, high-resolution probe of structure, bonding, protonation, and exchange dynamics in complex oxo systems such as polyoxometalates. In contemporary work, the most reliable insight arises from integrating ^{17}O NMR with diffraction, vibrational and X-ray spectroscopies, and DFT/AI modelling – thereby aligning local, oxygen-resolved information with ensemble (metal- or lattice-averaged) views of POM structure–reactivity.[26,74,77,87,89,91]

2.5 Practical optimisation strategies for ^{17}O NMR studies of polyoxometalates

Although the challenges associated with ^{17}O NMR spectroscopy, most notably its low natural abundance (0.037%) and pronounced quadrupolar broadening, are well recognised, recent methodological advances have established a practical and increasingly accessible toolkit for overcoming these limitations in polyoxometalate (POM) systems.[64,76,92]

2.5.1 Magnetic field strength. This remains one of the most impactful experimental parameters because second-order quadrupolar broadening decreases with increasing B_0, meaning ultrahigh-field NMR substantially improves resolution and aids separation of chemical-shift and quadrupolar contributions, especially for congested oxygen manifolds.[64,76,92]

2.5.2 Magic-angle spinning (MAS). MAS at fast to ultrafast rates (≥40–60 kHz, and increasingly ≥100 kHz) reduces anisotropic broadening and enables more efficient heteronuclear correlation experiments. In parallel, established multiple-quantum methods for half-integer quadrupolar nuclei (*e.g.*, MQMAS/STMAS) remain central for extracting high-resolution isotropic information and quadrupolar parameters (C_Q, η) from sites that are otherwise difficult to resolve.[28,64]

2.5.3 Isotopic enrichment strategies. These are also critical. Efficient ^{17}O-labelling approaches, particularly mechanochemistry-enabled routes and targeted $H_2{}^{17}O$ exchange, provide cost-effective access to labelled oxides and oxygen-bearing functional groups, enabling selective interrogation of structurally and catalytically relevant oxygen environments with reduced isotope consumption.[45,93]

2.5.4 DNP-enhanced solid-state NMR. For cases where enrichment is limited or where surfaces/dilute sites are targeted, DNP-enhanced solid-state NMR has emerged as a practical sensitivity-boosting route. Notably, DNP has been demonstrated to enable natural-abundance ^{17}O solid-state NMR, and indirect/heteronuclear detection strategies (*e.g.* ^{1}H–^{17}O HETCOR) and proton-detected experiments under fast MAS can extend the reach of ^{17}O NMR to challenging near-surface oxygen environments.[86,94,95]

2.5.5 DFT/GIPAW calculations. These are increasingly indispensable for robust spectral assignment, allowing experimental δ_{iso} and quadrupolar parameters to be correlated with local bonding, protonation states, and substitution patterns – thereby strengthening confidence in site-specific interpretation in complex inorganic solids.[96,97]

Additional optimisation strategies include site-biased enrichment (*e.g.*, selective and efficient ^{17}O-labelling routes), multi-field and variable-temperature measurements, pulse-sequence and excitation optimisation, sample–matrix engineering, multinuclear correlation experiments, and emerging machine-learning (ML) and AI-assisted analysis workflows.[20,93,98,99] Together, these approaches further enhance the reliability, sensitivity, and interpretative power of ^{17}O NMR, consolidating its evolution from a technically demanding technique into a robust and information-rich probe of polyoxometalate structure, dynamics, and reactivity.

3 Structural elucidations *via* ^{17}O NMR: case studies across POM archetypes

Fig. 7 summarises the multifaceted role of ^{17}O NMR spectroscopy in POM chemistry, highlighting its principal areas of application. In addition to serving as a powerful structural probe capable of discriminating terminal, bridging, and internal oxygen environments, ^{17}O NMR provides direct insight into protonation, hydration, and oxygen-exchange equilibria that underpin POM reactivity. When combined with isotopic labelling, variable-field and fast-MAS measurements, and DFT-based modelling, ^{17}O NMR evolves into an *operando*-capable technique for tracking catalytic oxygen-atom transfer (OAT) and redox processes within POM frameworks. Collectively, these capabilities enable ^{17}O NMR to bridge atomic-scale structure with functional transformations relevant to oxidation catalysis, water activation, and energy-conversion processes.

Building on the pioneering solution-state ^{17}O NMR studies of polyoxometalates by Klemperer and co-workers, which established feasibility and key sensitivity and assignment concepts in discrete metal-oxide clusters, subsequent advances in solid-state NMR, particularly ^{17}O magic-angle spinning (MAS) and high-resolution methods for quadrupolar nuclei, have enabled analogous site-resolved oxygen measurements in the solid phase.[11,12,14] Extensive later work has demonstrated that both ^{17}O chemical shifts and quadrupolar interaction parameters are highly sensitive to the local bonding geometry of M–O–M′ linkages. In oxide frameworks, landmark ^{17}O NMR studies such as those on titania gels, silicates, and related M–O–M networks, established clear correlations between δ_{iso}, C_Q/η, and structural descriptors including bond angle, bond length, and metal–oxygen covalency, with Ti–O–Ti linkages serving as a classic benchmark for interpreting bridging-oxygen environments.[17,25,100,101] These structure–NMR relationships have since been extended to a wide range of oxide and heterometallic systems and are increasingly strengthened by DFT-assisted analyses that directly relate trends in shielding and electric-field-gradient tensors to local electronic structure, including in mixed-metal polyoxometalates.[13] More recent ultrahigh-field (≥20 T) ^{17}O solid-state NMR further enhances the resolution of

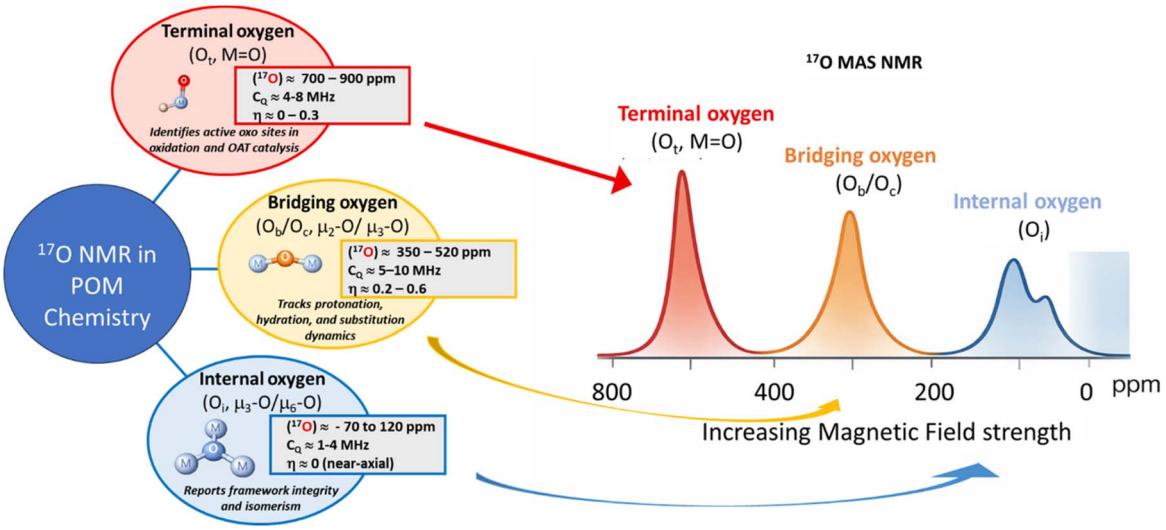

Fig. 7 Linking polyoxometalate (POM) structural oxygen motifs to characteristic ^{17}O MAS NMR observables. Terminal (O_t, M=O), bridging (O_b/O_c, μ_2–O), and internal (O_i, μ_3–O/μ_6–O) oxygen sites exhibit distinct ^{17}O chemical-shift ranges and quadrupolar parameters (C_Q, η), enabling site-specific discrimination of active oxo centres, protonation/hydration and substitution dynamics, and framework integrity or isomerism. The stylised ^{17}O MAS NMR spectrum (right) illustrates the corresponding high-, mid-, and low-ppm regions, highlighting how increased magnetic field strength improves resolution and facilitates structure–spectra correlations in POM chemistry.

inequivalent oxygen sites, improving the reliability of spectral assignments in complex metal–oxide materials containing multiple bridging oxygen environments.[74] Collectively, these insights have also informed broader applications of ^{17}O NMR in oxometalate chemistry, including catalysis.

3.1 Identifying bridging *vs.* terminal oxygens

^{17}O NMR spectroscopy directly probes the oxygen sublattice of oxometalate frameworks, allowing unambiguous assignment of terminal M=O (O_t), μ_2-and μ_3-bridging (O_b/O_c), and interior (O_i)

Table 3 Selected ^{17}O chemical-shift ranges in archetypal POMs[a]

POM type	Oxygen environment	^{17}O δ range (ppm)	Remarks	Ref.
Lindqvist $[W_6O_{19}]^{2-}$/M′W_5O_{18}	Terminal, O_t (W=O)	800–860	Very downfield W=O; axial/equatorial differentiation appears upon heterometal (M′) substitution	13, 15, 39 and 102
	Bridging μ_2–O (O_b) (W–O–W)	480–520	Cluster-belt μ_2-oxo; modest dependence on substitution/capping; typically, a single envelope near ∼500 ppm	13, 15 and 39
	Internal O_i (central μ_6–O)	−70 to −30	Strongly shielded; negative δ commonly observed (*e.g.*, μ_6–O ≈ −65 ppm in Nb-substituted analogues)	13, 39 and 103
Keggin $[PW_{12}O_{40}]^{3-}$	Terminal O_t (W=O)	760–770	Downfield O_t; small spread with counter-ion/solvent; useful fingerprint for heteroatom/isomer comparisons	13 and 15
	μ_2-bridging (O_b & O_c)	430–460	Two close sets (O_b/O_c) often partially resolved; sensitive to α/β isomerism and lacunary formation	13 and 15
	Internal O_i (μ_3 to W; "O_a" linked to P)	80–95	Inner framework oxygen(s) near heteroatom; most shielded of the three families in Keggin	13 and 15
Dawson $[P_2W_{18}O_{62}]^{6-}$	μ_2-bridging (O_b & O_c)	418–440	Several inequivalent μ_2-oxo; shifts track α_1/α_2 isomerism and site-specific substitution	15 and 104
	Terminal O_t (W=O)	738–760	Two close O_t sites (cap/belt) typically appear; slightly upfield from Keggin O_t in many media	15 and 104
	Internal O_i (μ_3 to W; near P)	75–106	Multiple inner oxygens; values sit in the strongly shielded regime	15 and 104

[a] Exact values vary with composition, solvent, counter-ions, T, and field; consult cited works for experimental conditions. For the Lindqvist line, we constrained the terminal range to W=O (thus 800–860 ppm) rather than including Mo- or Nb-based congeners (which shift O_t upfield). The μ_2-bridging and μ_6–O windows reflect the same sources and are robust across common counter-ions and media; local protonation, heteroatom substitution, and field/temperature can cause modest deviations.

Table 4 Site-resolved ^{17}O NMR chemical-shift windows for representative POMs.[a,b]

Entry	POM (family)	O_t (M=O) δ/ppm	μ_2-bridging (O_b/O_c) δ/ppm	Internal (O_i) δ/ppm	Notes	Ref.
1	$[W_6O_{19}]^{2-}$ (Lindqvist)	820–860	480–520	~70–95 (μ_6–O)	Classic W-Lindqvist; strong deshielding at O_t; μ_6–O most shielded	13 and 102
2	$[Mo_6O_{19}]^{2-}$ (Lindqvist)	700–780	430–500	~60–90 (μ_6–O)	Mo gives upfield O_t *vs.* W	13 and 102
3	$[Nb_6O_{19}]^{8-}$ (Lindqvist)	610–630	380–410	~70–90 (μ_6-O)	Exp. solution: μ_2–O ~393; O_t ~623; μ_6–O weak/near ~80	41 and 102
4	$[Ta_6O_{19}]^{8-}$ (Lindqvist)	~600–630	~380–410	~70–90 (μ_6–O)	Similar to Nb analogue	15 and 102
5	$[ZrW_5O_{18}]^{2-}$ (Lindqvist-derived)	800–860 (W=O)	470–520	—	Substitution perturbs O_t and C_Q	13
6	$[TiW_5O_{18}]^{3-}$ (Lindqvist-derived)	800–855 (W=O)	470–515	—	Non-aqueous syntheses; ^{17}O often *via* $H_2{}^{17}O$ swap	13 and 40
7	$[H_xNb_6O_{19}]^{(8-x)-}$ (Lindqvist, protonated)	600–630 (O_t)	360–400 (μ_2–O–H)	~70–90	Protonation shifts μ_2–O upfield/ downfield depending on site	41 and 102
8	$[PW_{12}O_{40}]^{3-}$ (Keggin)	760–770	430–460	80–95 (μ_3 to W; "O_i")	Benchmark Keggin fingerprints	13 and 15
9	$[SiW_{12}O_{40}]^{4-}$ (Keggin)	745–760	420–450	80–95	Heteroatom tunes O_i slightly	15
10	$[BW_{12}O_{40}]^{5-}$ (Keggin)	740–760	420–450	80–95	—	15
11	$[GeW_{12}O_{40}]^{4-}$ (Keggin)	745–760	420–450	80–95	—	15
12	$[AsW_{12}O_{40}]^{3-}$ (Keggin)	740–760	420–450	80–100	Inner O_i more sensitive to X	13 and 15
13	$[PMo_{12}O_{40}]^{3-}$ (Keggin)	630–690	360–420	60–85	O_t markedly upfield *vs.* W congeners	13 and 15
14	$[SiMo_{12}O_{40}]^{4-}$ (Keggin)	620–680	350–410	60–85	—	13 and 15
15	$[GeMo_{12}O_{40}]^{4-}$ (Keggin)	620–680	350–410	60–85	—	13
16	$[AsMo_{12}O_{40}]^{3-}$ (Keggin)	620–680	350–410	60–85	—	13
17	α-$[PW_{11}O_{39}]^{7-}$ (lacunary Keggin)	740–770 (O_t)	410–460	70–100	Lacunary sites broaden O_b/O_c window	13 and 102
18	α-$[SiW_{11}O_{39}]^{8-}$ (lacunary Keggin)	735–760	405–455	70–100	—	13
19	$[P_2W_{18}O_{62}]^{6-}$ (Dawson)	738–760	418–440	75–106	Multiple inequivalent μ_2–O resolved at high field	13 and 15
20	$[As_2W_{18}O_{62}]^{6-}$ (Dawson)	730–755	415–440	75–110	O_i sensitive to heteroatom	13
21	$[Se_2W_{18}O_{62}]^{6-}$ (Dawson)	730–755	415–440	75–110	Seleno-Dawson congeners similar to As_2	13
22	$[P_2Mo_{18}O_{62}]^{6-}$ (Dawson)	610–690	360–420	60–95	Mo shifts upfield *vs.* W	13 and 15
23	α_1-$[P_2W_{18}O_{62}]^{6-}$ (Dawson isomer)	738–760	418–440	80–105	O_b/O_c split tracks α_1/α_2	13 and 15
24	α_2-$[P_2W_{18}O_{62}]^{6-}$ (Dawson isomer)	738–760	418–440	75–100	Slightly different O_i pattern	13 and 102
25	$[Nb_{10}O_{28}]^{6-}$ (decaniobate; related)	(No O_t)	350–420	~80–100 (μ_6-like in derived species)	Included for μ–O window *vs.* Lindqvist	15 and 41
26	$[PVW_{11}O_{40}]^{5-}$ (mono-V Keggin)	740–770 (W=O), 840–900 (V=O)	420–460	80–95	V=O often further downfield than W=O	13
27	$[PMo_{11}VW_1O_{40}]^{4-}$ (mixed Keggin)	630–900 (O_t mix)	360–470	60–100	Mixed addenda broaden O_t band	13
28	$[SiW_{11}TiO_{40}]^{6-}$ (Ti-substituted Keggin)	735–765 (W=O)	410–455	75–100	Substitutions bias O_b/O_c	13
29	$[P_2W_{17}MoO_{62}]^{6-}$ (mixed Dawson)	700–760 (O_t mix)	390–440	70–105	Mixed Mo/W pattern	13

Table 4 (*Contd.*)

Entry	POM (family)	O_t (M=O) δ/ppm	μ_2-bridging (O_b/O_c) δ/ppm	Internal (O_i) δ/ppm	Notes	Ref.
30	$[P_2W_{17}VO_{62}]^{7-}$ (V-doped Dawson)	740–900 (O_t mix)	410–450	80–110	V=O contributes most downfield O_t	13
31	$[SiW_{11}ZrO_{40}]^{6-}$ (Zr-Keggin)	735–760 (W=O)	410–455	75–100	Zr affects O_b/O_c connectivity	13
32	$[H_3PW_{12}O_{40}]$ (Keggin acid)	750–770	430–460 (broader)	80–95	Protonation subtly shifts O_b/O_c; counter-ion effects	11 and 15
33	$[H_3PMo_{12}O_{40}]$ (Keggin acid)	620–680	350–410 (broader)	60–85	Mo acid analogue	11 and 15
34	$[HNb_6O_{19}]^{7-}$ (Lindqvist, mono-H)	605–630	360–395 (μ_2-O–H)	~70–90	^{17}O confirms proton at μ_2–O	105
35	$[AlW_{12}O_{40}]^{5-}$ (Keggin)	740–770	420–460	80–95	Al heteroatom; W addenda	13
36	$[GaW_{12}O_{40}]^{5-}$ (Keggin)	740–770	420–460	80–95	—	13
37	$[SbW_{12}O_{40}]^{3-}$ (Keggin)	740–765	420–455	80–95	Heavier X shifts O_i slightly	13
38	$[BiW_{12}O_{40}]^{3-}$ (Keggin)	740–765	420–455	80–95	—	13
39	$H_4[SiW_{12}O_{40}]$ (Keggin acid)	745–765	425–455	80–95	Protonation broadens O_b/O_c	15
40	$H_5[BW_{12}O_{40}]$ (Keggin acid)	740–760	420–450	80–95	—	15
41	$[PV_2W_{10}O_{40}]^{5-}$(mixed Keggin)	W=O 735–765; V=O 840–915	420–460	80–95	Two V=O sets possible	13
42	$[PV_3W_9O_{40}]^{6-}$ (mixed Keggin)	V=O 845–920	420–460	80–95	V-rich O_t band	13
43	$[FePW_{11}O_{39}]^{5-}$ (Keggin lacunary, Fe-sub.)	735–765	415–455	80–95	TM at vacant site; O windows Keggin-like	15
44	$[CoPW_{11}O_{39}]^{5-}$ (Substituted -lacunary Keggin)	735–765	415–455	80–95	—	15
45	$[NiPW_{11}O_{39}]^{5-}$(Substituted -lacunary Keggin)	735–765	415–455	80–95	—	15
46	$[CuPW_{11}O_{39}]^{5-}$(Substituted -lacunary Keggin)	735–765	415–455	80–95	—	15
47	$[ZnPW_{11}O_{39}]^{5-}$ (Substituted -lacunary Keggin)	735–765	415–455	80–95	—	15
48	$[TiPW_{11}O_{39}]^{(5-6)-}$ (Substituted -lacunary Keggin)	735–765 (W=O)	415–455	80–95	Ti at lacuna; subtle O_b/O_c shifts	13
49	$[ZrPW_{11}O_{39}]^{(5-6)-}$ (Substituted -lacunary Keggin)	735–765	415–455	80–95	—	13
50	$[SnPW_{11}O_{39}]^{(4-5)-}$ (Substituted-lacunary Keggin, *e.g.*, –Cl/–OR)	735–765	415–455	80–95	^{17}O windows for sub. Sn at lacuna	36 and 37
51	$[As_2W_{17}VO_{62}]^{7-}$ (Mixed Dawson)	730–900	410–445	80–110	—	13
52	$[Se_2W_{17}VO_{62}]^{7-}$ (Mixed Dawson)	730–900	410–445	80–110	—	13
53	$[P_2Mo_{17}WO_{62}]^{6-}$ (Mixed Dawson)	620–760	360–440	65–105	Mo-rich upfield O_t	15
54	$H_6[P_2W_{18}O_{62}]$ (Dawson acid)	735–760	415–440	75–105	Protonation broadens O_b/O_c	13
55	$[P_2W_{15}V_3O_{62}]^{9-}$ (Mixed Dawson)	735–915	410–445	80–110	Multiple V=O components	13
56	$[P_2W_{17}O_{61}]^{10-}$ (Mono-lacunary Dawson)	735–760	410–445	75–105	More distinct μ–O sets	13
57	$[As_2W_{17}O_{61}]^{10-}$ (Mono-lacunary Dawson)	730–755	410–445	75–110	—	13

Table 4 (*Contd.*)

Entry	POM (family)	O_t (M=O) δ/ppm	μ_2-bridging (O_b/O_c) δ/ppm	Internal (O_i) δ/ppm	Notes	Ref.
58	$[Se_2W_{17}O_{61}]^{10-}$ (Mono-lacunary Dawson)	730–755	410–445	75–110	—	13
59	$[(\mu\text{-O})(TiW_5O_{18})_2]^{6-}$ (Lindqvist dimer)	800–855 (W=O)	470–515	μ–O bridge distinct	Widely studied by ^{17}O	103
60	$[ZrW_5O_{18}]^{3-}$ (Lindqvist derived)	800–855 (W=O)	470–515	—	—	40
61	$\{(\mu\text{-MeO})ZrW_5O_{18}\}_2^{6-}$ (Lindqvist dimer)	800–855	470–515	μ–MeO/μ–HO resolved	—	40
62	$[HfW_5O_{18}]^{3-}$ (Lindqvist derived)	800–855	470–515	—	—	13
63	$[SnW_5O_{18}]^{3-}$ (Lindqvist derived)	800–855	470–515	—	—	103
64	$\{(\mu\text{–O})SnW_5O_{18}\}_2^{6-}$ (Lindqvist dimer)	800–855	470–515	μ–O distinctive	Less stable than Ti analogue	103
65	$[(^iPrO)TiMo_5O_{18}]^{3-}$ (Lindqvist derived)	620–700 (Mo=O), 780–820 (Ti=O if present)	350–420	−40 to 0 (μ_6 in Mo_5 core)	Ti–Mo family	106
66	$[SnMo_5O_{18}]^{3-}$ (Lindqvist derived)	620–690	350–420	−40 to 0	—	106
67	$[ZrMo_5O_{18}]^{3-}$ (Lindqvist derived)	620–690	350–420	−40 to 0	—	106
68	$[PV_2Mo_{10}O_{40}]^{5-}$ (Mixed Keggin)	Mo=O 620–680; V=O 840–910	350–420	60–85	Mixed addenda	15
69	$[PVMo_{11}O_{40}]^{4-}$ (Mixed Keggin)	620–900 (Mixed O_t)	350–420	60–85	One V=O band	15
70	$[AsMo_{12}O_{40}]^{3-}$ (Keggin)	620–680	350–410	60–85	—	13
71	$[SbMo_{12}O_{40}]^{3-}$ (Keggin)	620–680	350–410	60–85	—	13
72	$[BiMo_{12}O_{40}]^{3-}$ (Keggin)	620–680	350–410	60–85	—	13
73	$[AlMo_{12}O_{40}]^{3-}$ (Keggin)	620–680	350–410	60–85	—	13
74	$[GaMo_{12}O_{40}]^{3-}$ (Keggin)	620–680	350–410	60–85	—	13
75	$[BMo_{12}O_{40}]^{5-}$ (Keggin)	620–680	350–410	60–85	—	15
76	$[BW_{11}O_{39}]^{9-}$ (lacunary Keggin)	735–765	410–455	75–100	Lacunary broadening of O_Q/O_c	13
77	$[GaW_{11}O_{39}]^{9-}$ (Lacunary Keggin)	735–765	410–455	75–100	—	13
78	$[AlW_{11}O_{39}]^{9-}$ (Lacunary Keggin)	735–765	410–455	75–100	—	13
79	$[BiW_{11}O_{39}]^{7-}$ (Lacunary Keggin)	735–765	410–455	75–100	—	13
80	$[(HO)TiW_5O_{18}]^{3-}$ (Substituted lacunary Lindqvist)	800–855	470–515	—	Hydroxido variant	103
81	$[(HO)SnW_5O_{18}]^{3-}$ (Substituted lacunary Lindqvist)	800–855	470–515	—	—	103
82	$[O{=}TiW_5O_{18}]^{4-}$ (Titanyl Lindqvist)	830–870 (Ti=O + W=O)	470–515	—	Terminal Ti=O seen	103
83	$\{(\mu\text{–O})(TiW_5O_{18})_2(dmso)\}^{4-}$ (Lindqvist dimer adduct)	800–855	470–515	—	Adduct characterised by ^{17}O	103
84	$\{(\mu\text{–O})(TiW_5O_{18})_2(SnMe_2)\}^{4-}$ (Lindqvist dimer adduct)	800–855	470–515	—	Electrophile binding at Ti–O–W	103
85	$[PV_3Mo_9O_{40}]^{6-}$ (Mixed Keggin)	Mo=O 620–680; V=O 845–915	350–420	60–85	V-rich O_t	15
86	$[SiW_{11}SnO_{40}]^{6-}$ (Substituted lacunary Keggin)	735–765	410–455	75–100	—	13

Table 4 (*Contd.*)

Entry	POM (family)	O_t (M=O) δ/ppm	μ_2-bridging (O_b/O_c) δ/ppm	Internal (O_i) δ/ppm	Notes	Ref.
87	$[GeW_{11}TiO_{40}]^{6-}$ (Substituted lacunary Keggin)	735–765	410–455	75–100	Ge *vs.* Si subtle O_i shift	15
88	$[GeW_{11}ZrO_{40}]^{6-}$ (Substituted lacunary Keggin)	735–765	410–455	75–100	—	15
89	$[GeW_{11}SnO_{40}]^{6-}$ (Substituted lacunary Keggin)	735–765	410–455	75–100	—	15
90	$[H_4SiMo_{12}O_{40}]$ (Keggin)	620–680	350–410	60–85	—	15
91	$[As_2Mo_{18}O_{62}]^{6-}$ (Dawson)	610–690	360–420	60–95	—	13
92	$[Se_2Mo_{18}O_{62}]^{6-}$ (Dawson)	610–690	360–420	60–95	—	13
93	$[(L)MPW_{11}O_{39}]^{n-}$ (Substituted Lacunary Keggin, L = Cl, OH, CH_3O; M = Sn, Pb, Bi, Sb, Ti)	735–765	410–455	75–100	^{17}O-enriched precursor used to build Sn, Pb, Bi, Sb, Ti series	37

[a] Values are grouped by oxygen type: terminal M=O (O_t), μ_2-bridging (O_b/O_c), and interior O (O_i; μ_3 or μ_6) across Lindqvist, Keggin, Dawson, and selected substituted/lacunary derivatives. Chemical shifts are referenced to H_2O(l) = 0 ppm unless stated otherwise. Ranges reflect literature values and may vary with field strength, temperature, solvent/phase, counter-ions, heteroatom substitution, isomerism (*e.g.*, α_1/α_2 Dawson), and protonation state. [b] "—" means no special notes.

Fig. 8 Typical binding modes in (a) Lindqvist-type and (b) Keggin and Wells-Dawson-type POMs. White spheres are oxygen atoms. The figure and the caption are reproduced from ref. 13. Copyright 2014, Royal Society of Chemistry.

sites. In Keggin-type POMs (*e.g.*, $[PW_{12}O_{40}]^{3-}$), ^{17}O chemical shifts act as robust fingerprints for diagnosing isomerism and heteroatom substitution.[11,13] The O_t sites typically resonate far downfield (≈760–770 ppm for $[PW_{12}O_{40}]^{3-}$),[13,15] consistent with strong M=O multiple-bond character and reduced shielding, whereas μ_2-bridging O_b and interior O_i sites appear progressively upfield with positions modulated by connectivity, protonation, heteroatom identity, hydration, and counter-cations. Table 3 compiles practical ^{17}O "fingerprints" for the three archetypal POM families: Lindqvist, Keggin, and Dawson, organised by oxygen type (terminal M=O, μ_2-bridging, interior μ_3/μ_6) and referenced to H_2O(l) = 0 ppm. It highlights the characteristic downfield O_t band in W-based clusters, the mid-field μ_2-bridging O_b/O_c envelope, and the strongly shielded O_i sites, including the well-known negative shifts of μ_6–O in Lindqvist anions. The table also notes where symmetry/isomerism (*e.g.*, α_1/α_2 Dawson) and lacunary formation split or bias these windows, providing fast, literature-anchored guidance for site assignment across derivatives. Because ^{17}O shifts are sensitive to protonation, substitution, medium, temperature, and field and because quadrupolar parameters (C_Q, η) shape linewidths, these windows should be used as assignment guides alongside complementary 2D/multi-field experiments and, where appropriate, DFT calibration. In the assignments, multi-field/fast-MAS experiments and line-shape analyses (extracting δ_{iso}, C_Q, η) enable confident resolution of overlapping sites; 2D methods (MQMAS/STMAS; ^{1}H–^{17}O HETCOR; heteronuclear recoupling) further decouple anisotropy from isotropic shifts to deliver site-resolved maps across Lindqvist, Keggin, and Dawson families. For Dawson-type and Lindqvist clusters, ^{17}O NMR has also exposed local distortions and substitution effects, while theory benchmarks rationalize the observed trends, typically, O_t shifts track M–O bond order, and O_b/O_i shifts follow electron density and local symmetry.[13,15]

Table 4 extends these fingerprints for rapid comparison of representative members across families and substitutions. In tungsten-rich systems, terminal W=O (O_t) commonly appears far downfield (≈740–860 ppm), μ_2-bridging O_b/O_c occupy a mid-field region (≈350–460/480–520 ppm depending on Mo *vs.* W), and interior O_i are most shielded (≈60–110 ppm for μ_3 in Keggin/Dawson and often negative for μ_6 in Lindqvist). Again, because both δ and the quadrupolar terms (C_Q, η) govern the spectra, the listed ranges are best treated as practical guides

Table 5 Selected case studies of ^{17}O NMR applications in polyoxometalate chemistry[a]

S/N	POM type/system/method	^{17}O NMR techniques	^{17}O NMR insights	Catalytic/structural implication	Ref.
1	Keggin $[PW_{12}O_{40}]^{3-}$	MAS	O_t *vs.* μ–O_b resolved; δ windows established	Fingerprint library for Keggin assignments	12
2	$[PW_{12-x}M_xO_{40}]^{n-}$ (M = Ti, Nb, Pd)	MQMAS, HETCOR	Substitution-specific $\delta(^{17}O)$ perturbations near M site	Mapping heterometal location; acidity tuning	108
3	$[P_2W_{18}O_{62}]^{6-}$ (Dawson)	MQMAS, static high-field	μ–O_b manifolds separated; isomer sensitivity	Distinguishing α_1/α_2; structure–function links	104
4	V-substituted Dawson $[P_2VW_{17}O_{62}]^{7-}$	HETCOR, DFT	Substitution followed at μ–O adjacent to V^V	Redox/catalysis modulation *via* V incorporation	109
5	$[W_6O_{19}]^{2-}$ (Lindqvist)	Static MAS	Clear O_t *vs.* μ–O; distortion metrics from C_Q	Baseline for M′W_5 substitutions	39
6	(MeO)Sn$W_5O_{18}^{3-}$ (Sn-Lindqvist)	MAS	Capping perturbs nearby O_t; distinct δ pattern	Reactivity of SnW_5 anions; ligand effects	110
7	Decatungstate $[W_{10}O_{32}]^{4-}$	MQMAS	Site-resolved ^{17}O with Ln adducts	Photocatalysis-relevant oxygen mapping	111
8	Mixed-metal Mo/W Keggin series	MAS, DFT	Trends in $\delta(^{17}O)$ *vs.* metal identity/connectivity	Electronic structure descriptors for design	13
9	Polyoxomolybdates in solution	Variable-T MAS	^{17}O dispersions *vs.* protonation; dynamics	Acid–base speciation pathways	12
10	Paratungstate/Heptatungstate	Solution NMR	Distinct solution ^{17}O signatures across isomers	Speciation under hydrothermal/aqueous conditions	112
11	Nb/Ta oxo-clusters	MAS	Early $\delta(^{17}O)$ libraries; sensitivity to bonding	Framework for modern mixed-metal POM work	11
12	Keggin redox series (DFT-aided)	DFT-aided MAS	Computed *vs.* experimental $\delta(^{17}O)$ correlations	Predictive assignment in complex spectra	15
13	Polyoxotungstate clusters (DFT)	MQMAS	Terminal *vs.* bridging trends reproduced	Validating substitution/protonation effects	102
14	Discrete metal-oxide clusters	HETCOR, DFT	Best-practice assignments; solution–solid links	Roadmap for ^{17}O in POMs	14
15	Keggin isomer discrimination	MQMAS	δ/C_Q changes quantify $\alpha/\beta/\gamma$ forms	Targeted synthesis & property control	13
16	Dawson chiral forms with Ln^{III}	Variable-T MAS + ^{183}W	Temperature-dependent NMR (with ^{183}W) supports ^{17}O patterns	Dimerization/assembly in water	113
17	POM speciation under exchange	^{17}O-labeling/exchange	$H_2{}^{17}O$ labelling strategies summarized	Efficient enrichment for site-specific study	10, 41, 44 and 114
18	Non-aqueous POM synthesis	MAS	Minimal $H_2{}^{17}O$ routes to enriched POMs	Cost-effective isotopic labelling	39
19	Virtual lacunary pentatungstate chemistry	ESI-MS + ^{17}O NMR	Combined ^{17}O/ESI-MS to track transformations	Mechanisms of cluster rearrangement	114
20	Oxo-replaced POMs (O → F, *etc.*)	MAS, DFT	^{17}O contrasts upon oxo replacement	Tuning electron density & reactivity	1
21	Polyoxovanadates	^{17}O–^{51}V HETCOR	$\delta(^{17}O)$ *vs.* V content/coupling to ^{51}V	Mixed-metal speciation guidelines	115
22	Decatungstate ionic liquids	DNP-MAS	Environment-dependent shifts (with ^{183}W support)	Media effects on oxygen sites	116
23	Paramagnetic POMs	MAS	Linear correlations in $\delta(^{17}O)$ across series	Interpreting paramagnetic shift components	117
24	Electron-rich POMs (bipolaron)	High-field MQMAS	^{17}O detects charge-delocalization changes	Redox-active catalysis design	118
25	General POM materials	MQMAS, STMAS, HETCOR	MQMAS/STMAS/HETCOR exemplars	Toolkit for complex POM spectra	21 and 94
26	High-field (≥28 T) ^{17}O MAS (methods)	High-field MAS	Field-dependent ^{17}O resolution in solids	Strategy for congested POM spectra	21
27	^{17}O DNP in oxides (methods)	DNP-MAS	Orders-of-magnitude sensitivity gains	Enables dilute/enriched-limited POM studies	52–54, 94 and 119
28	^{17}O in discrete clusters	MAS	Survey of Keggin/Dawson/Lindqvist cases	Best practices, pitfalls	14
29	Theoretical chem-shift atlas	DFT-GIPAW	Systematic $\delta(^{17}O)$ *vs.* structure/connectivity	Assignment aid across POM families	13
30	DFT protocol assessment	DFT	Hybrid functionals needed for accuracy	Reliable prediction of O_t *vs.* μ–O_b	15
31	Polyoxometalates chemistry	Review/*meta*-analysis	Context for ^{17}O case data	Links structure to function broadly	120
32	Polyoxoniobate rings	MAS	Early ^{17}O fingerprints in Nb systems	Extends beyond W/Mo chemistry	11
33	^{183}W/^{17}O cross-validation	^{17}O–^{183}W HETCOR	Consistency of oxygen assignments	Robust multi-nuclear strategies	102
34	Dawson: V-substitution kinetics	*In situ* MAS	*In situ* speciation + NMR	Synthesis control for active sites	109
35	Heptatungstate ↔ paratungstate	Variable-T MAS	Distinct solution ^{17}O signatures	Monitoring interconversion pathways	112
36	Keggin with heteroatom Sn/Ge/Ru	HETCOR, DFT	Neighbouring O shifts diagnose incorporation	Tailoring redox & acidity	108
37	Ln-decatungstate solution sets	MQMAS	Site patterning with Ln^{III}	Photocatalysis/electrochemistry links	111

Table 5 (*Contd.*)

S/N	POM type/system/method	^{17}O NMR techniques	^{17}O NMR insights	Catalytic/structural implication	Ref.
38	Keggin charge-state effects	Variable-field MAS	$\delta(^{17}O)$ *vs.* overall charge; hydration	Counter-ion & medium influences	13
39	POM rearrangements ($SiW_{11} \rightarrow SiW_{10}$)	DNP-MAS + ESI-MS	^{17}O tracks lacunary rearrangement	Pathways to active lacunary motifs	114
40	Mixed-metal W/Mo series	MQMAS, DFT	$\delta(^{17}O)$ trends validate bonding models	Guides selection of frameworks	117

[a] Each entry lists the POM system, the key ^{17}O-specific insight (*e.g.*, $O_t/O_b/O_i$ resolution, heterometal mapping, protonation/exchange dynamics, multi-field/MQMAS/HETCOR readouts), the catalytic or structural implication (*e.g.*, isomer discrimination, redox tuning, photocatalytic function), and the primary source.

and the cited sources should be consulted when matching specific compositions and conditions.

3.2 Probing isomerism and substitution effects

Isomerism (*e.g.*, $\alpha/\beta/\gamma$ in Keggin and α_1/α_2 in Dawson) reorganises M–O connectivities and hydrogen-bond networks, giving diagnostic ^{17}O signatures. Small symmetry changes alter both δ_{iso} and C_Q, so multi-field measurements (ideally $\geq$20 T) are powerful for separating chemical-shift *vs.* second-order quadrupolar contributions and for comparing isomers quantitatively. Heteroatom substitution (*e.g.*, V^{v}, Nb^{v}, Ti^{iv}, Sn^{iv}, Ru^{ii} at lacunary sites and framework substitutions) often causes selective perturbations, most conspicuously at nearby O_t and μ–O positions, enabling mapping of substitution sites and local distortions. DFT studies (cluster and periodic GIPAW) now reproduce experimental trends across polyoxotungstates, polyoxomolybdates, and mixed-metal derivatives, providing predictive guidance when peaks overlap.[13] To visualize how structural isomerism reorganises metal–oxygen connectivities and affects ^{17}O NMR signatures, the representative binding modes of polyoxometalate (POM) frameworks are illustrated in Fig. 8. The diagram compares the coordination geometries in Lindqvist-, Keggin-, and Wells–Dawson-type architectures, highlighting the distinct arrangements of terminal (M═O), bridging (M–O–M), and internal (X–O–M) oxygen atoms. Subtle reorientations of these M–O linkages underpin the $\alpha/\beta/\gamma$ (Keggin) and α_1/α_2 (Dawson) isomeric transformations, which give rise to characteristic differences in δ_{iso} and C_Q values observed in ^{17}O NMR spectra.

3.3 Case studies in Lindqvist, Keggin, and Dawson clusters

3.3.1 Lindqvist. In $[W_6O_{19}]^{2-}$ and $M'W_5O_{18}$-type anions (*e.g.*, alkoxido-Sn substituted), ^{17}O tracks local symmetry breaking and capping effects. Selective enrichment strategies (using minimal $H_2{}^{17}O$) plus high-field/fast-MAS experiments enable unambiguous separation of O_t *vs.* μ–O resonances and quantification of distortion about the substituted site.[39]

3.3.2 Keggin. Early solution studies established the wide ^{17}O shift dispersion in Mo/W Keggin ions and linked O_t downfield positions to multiple-bond character. More recent combined ^{17}O/DFT work extended this to heterometal-substituted $[PW_{12-x}M_xO_{40}]^{n-}$ families, revealing linear free-energy-like relationships between computed shielding and M–O bond metrics.[11–13,58,107]

3.3.3 Dawson. For $[P_2W_{18}O_{62}]^{6-}$ and derivatives, ^{17}O NMR resolves symmetry-inequivalent O_b manifolds that respond sensitively to α_1/α_2 isomerism and to metal substitution at lacunary sites. Complementary ^{183}W/^{31}P and Raman data help anchor assignments, but ^{17}O provides the decisive site-selective handle on O environments adjacent to the substituted centers.[104] Table 5 synthesises representative applications of ^{17}O NMR across Lindqvist, Keggin, Dawson, and related polyoxometalate motifs, spanning both solution and solid-state studies. The cases illustrate how site-resolved ^{17}O fingerprints (O_t *vs.* μ-bridging *vs.* interior O) enable isomer identification, locate heterometal substitutions, quantify protonation and

$H_2{}^{17}O$ exchange kinetics, and monitors framework rearrangements. This often has direct consequences for redox behaviour, acidity, and catalytic performance (*e.g.*, O-atom transfer and photocatalysis). These applications utilise methods such as high-field MAS with MQMAS/STMAS and ^1H–^{17}O HETCOR for congestion relief and distance information, as well as isotopic-labelling strategies and DFT-assisted assignments that convert complex spectra into practical structural information.

Across Lindqvist, Keggin, and Dawson archetypes, ^{17}O NMR, augmented by targeted ^{17}O labeling, multi-field/2D (MQMAS/STMAS, ^1H–^{17}O HETCOR) experiments, and DFT, delivers fast, site-resolved fingerprints ($O_t/O_b/O_i$), quantifies isomerism and substitution effects, and tracks protonation/hydration/exchange *in situ*, thereby linking atomic-scale oxygen structure directly to catalytic OAT pathways and redox function.

4 Insights into dynamics and reactivity from ^{17}O NMR

POMs are dynamic – exchanging protons, water, and (in oxidising media) peroxo ligands. These motions underpin acid–base chemistry, redox activity, and oxygen-atom transfer (OAT) reactivity.[10] ^{17}O NMR, by directly observing oxygen nuclei provides time- and site-resolved views of protonation, hydration, and oxygen exchange that are difficult to access with any other method[14] In both solution and solids, ^{17}O chemical shifts (δ_{iso}), quadrupolar parameters (C_Q, η), and relaxation/exchange observables (T_1, T_2, line shapes) provide information on local bonding, hydrogen bonding, and exchange kinetics[41] When combined with multi-field/fast-MAS measurements, 2D ^1H–^{17}O correlation, dynamic studies (EXSY/EXSY-like), and DFT, one can map pathways for hydrolysis/condensation, locate basic or protonated oxygens, follow insertion/removal of peroxo groups, and even monitor site-selective O exchange with solvent water during catalytic turnover.[10,13,94,121]

Fig. 9 and 10 collectively illustrate the dynamic oxygen-exchange and redox behaviour that underpins oxygen-atom transfer (OAT) chemistry in polyoxometalate-like and transition-metal oxo systems. Fig. 9 depicts representative oxidants and catalytic peroxo intermediates that mediate O-atom transfer and ligand exchange in oxidising media, while Fig. 10 demonstrates how ^{17}O NMR parameters (δ_{iso}, C_Q, η) sensitively report on the local electronic structure and reactivity of these species. These provide sound support that ^{17}O NMR provides a direct, time- and site-resolved probe of protonation, hydration, and peroxo insertion/removal processes, linking measurable spectroscopic parameters to fundamental pathways of hydrolysis, condensation, and catalytic oxygen exchange.

4.1 ^{17}O NMR for probing protonation, hydration, and exchange processes

4.1.1 Protonation states and hydrogen bonding. Protonation reorganises the oxygen lattice in POMs. Bridging oxygens (μ_2–O, μ_3–O) are generally the most basic, protonating first and producing marked upfield shifts in $\delta(^{17}O)$ and modest decreases in quadrupolar coupling constants (C_Q) and asymmetry parameters (η). In contrast, terminal M=O groups remain unprotonated until strongly acidic conditions. Classic ^{17}O solution studies on iso- and heteropolyanions established these trends, showing that acidification drives upfield motion of characteristic oxygen resonances and identifies the most basic lattice sites; modern works extend these observations across W/Mo/V frameworks.[12,14] In practical terms, $\delta(^{17}O)$ variations of tens to hundreds of ppm, coupled with line-width broadening, reflect local protonation and hydrogen-bonding effects across O_t, μ–O, and O_i sites.

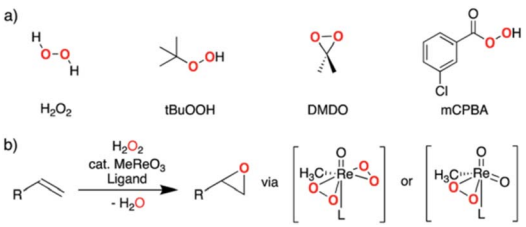

Fig. 9 Peroxide oxidants and peroxo-mediated epoxidation pathway. (a) Representative primary peroxide oxidants used for electrophilic epoxidation, (b) MTO-catalyzed olefin epoxidation involving bis-peroxo- or monoperoxo-species (L = pyridine or water). Reproduced from ref. 122. Copyright 2019, Royal Society of Chemistry.

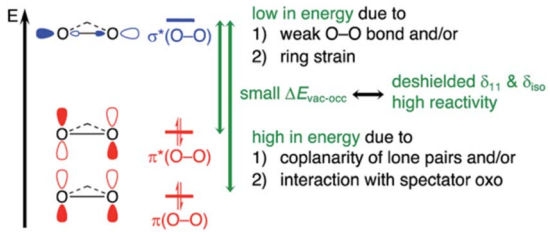

Fig. 10 ^{17}O NMR as an electronic-structure probe for epoxidation catalysis. Reproduced from ref. 122. Copyright 2019, Royal Society of Chemistry.

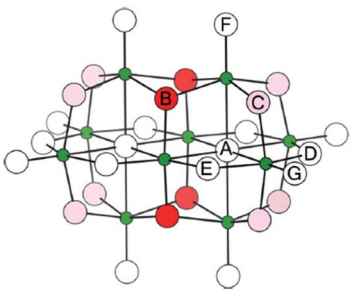

Fig. 11 Site-labelled oxygen lattice in a POM (decavanadate, $[V_{10}O_{28}]^{6-}$) highlighting that bridging μ–O sites protonate first, producing upfield $\delta(^{17}O)$ and altered C_Q/η, whereas terminal V=O remain unprotonated until strongly acidic conditions; ^{17}O NMR thus localizes protonation and captures exchange-averaged behaviour under acidification. (A) V_6O; (B) V_3O; (C–E) V_2O; (F and G) VO. Red and pink colours identify a 60% and 40% degree of protonation in sites B and C in $[HV_{10}O^{28}]^{5-}$. Reproduced from ref. 13. Copyright 2014, Royal Society of Chemistry.

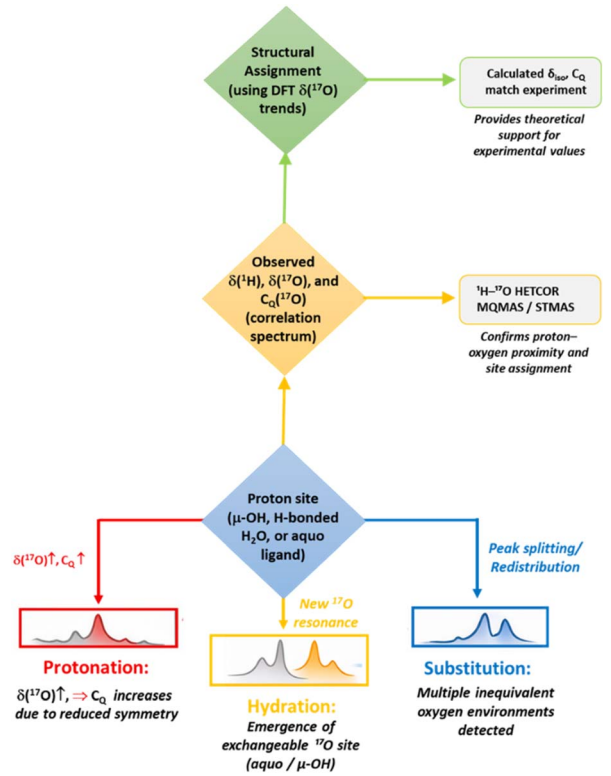

Fig. 12 Mechanistic interpretation of protonation, hydration, and substitution processes in POMs using ^{17}O NMR observables. The scheme illustrates how changes at proton sites (μ–OH, hydrogen-bonded H_2O, or aquo ligands) propagate to experimentally observed ^{1}H and ^{17}O chemical shifts (δ) and ^{17}O quadrupolar parameters (C_Q) in correlation spectra (^{1}H–^{17}O HETCOR, MQMAS/STMAS). Indicative ^{17}O MAS NMR spectral insets show characteristic responses to protonation (downfield shift and increased quadrupolar broadening), hydration (emergence of new exchangeable ^{17}O resonances), and substitution or isomerisation (peak splitting and intensity redistribution). Structural assignment is achieved by comparison with DFT-calculated δ_{iso} and C_Q values, closing the experiment–theory loop for site-specific mechanistic analysis.

^{17}O NMR is particularly sensitive to hydrogen bonding, and its integration with ^{1}H–^{17}O correlation experiments provide direct structural insight into the position and environment of protons in hydrated or hybrid POMs. At high magnetic fields (≥28–35 T) and fast MAS, proton-detected ^{1}H → ^{17}O HETCOR and D-RINEPT experiments discriminate overlapping oxygen sites by the chemical shifts of their associated protons, mapping hydrogen-bond topologies and acid–base equilibria.[73,122]

Fig. 11 illustrates how protonation reorganises the oxygen sublattice in the decavanadate anion, $[V_{10}O_{28}]^{6-}$, and how these structural changes manifest in measurable ^{17}O NMR parameters. Bridging oxygens (μ_2–O, μ_3–O) accept protons first, leading to upfield $\delta(^{17}O)$ shifts ($\Delta\delta \approx -30$ to -200 ppm) and reduced C_Q values corresponding to enhanced local shielding. DFT models reproduce these behaviours, showing M–O bond elongation (~0.15–0.17 Å) upon protonation and correlated $\delta(^{17}O)$ displacements of several hundred ppm. Adjacent non-protonated sites exhibit smaller downfield responses due to electronic redistribution within M–O–M bridges. Under rapid proton exchange, coalesced resonances emerge, reflecting dynamic averaging among equivalent μ–O positions.[13,58,123–126]

Complementing this discussion, Fig. 12 schematically illustrates the ^{1}H–^{17}O correlation-based workflow used to identify and assign proton-bearing oxygen sites in polyoxometalates. Starting from proton-containing environments (μ–OH, hydrogen-bonded H_2O, or aquo ligands), ^{1}H–^{17}O correlation spectra (^{1}H–^{17}O HETCOR, MQMAS/STMAS) provide simultaneous access to $\delta(^{1}H)$, $\delta(^{17}O)$, and ^{17}O quadrupolar parameters (C_Q), revealing characteristic spectral responses associated with protonation, hydration, and substitution. Comparison of these experimentally derived parameters with DFT-predicted $\delta(^{17}O)$ trends enables robust, site-specific structural assignment of hydroxylated and hydrated motifs within POM frameworks. By explicitly linking mechanistic transformations to their spectral fingerprints, this integrated experimental–computational approach affords a direct view of protonation, hydrogen bonding, and exchange processes that govern POM reactivity[127] and catalysis.

4.1.2 Hydration and water organisation. Hydration dynamics play a central role in defining the structure, proton mobility, and redox activity of POMs. Whether in solution, ionic liquids, or solids, hydration layers around POMs strongly modulate oxygen shifts and quadrupolar parameters. ^{17}O can resolve lattice, coordinated, and interstitial water in POM-containing solids (and related oxo clusters), especially when combined with ^{1}H detection under fast MAS. These methods, developed broadly in solid-state ^{17}O NMR, translate directly to hydrated POM salts, POM–MOF hosts, and surface-grafted POM films.[50] In solution, ^{17}O NMR remains the most direct nucleus for following oxygen-bearing solvent interactions, complementing ^{31}P/^{183}W probes that reflect the metal/heteroatom environment. Speciation over pH, concentration, counter-cation, and buffer identity, now systematically mapped for widely used POMs provides essential context for dynamic ^{17}O assignments in water.[10]

In the ^{17}O NMR view (Fig. 13), distinct hydration motifs can be resolved depending on whether water molecules are directly coordinated to the metal centers or located in the outer-sphere hydrogen-bond network. Coordinated H_2O molecules often engage in rapid μ–OH exchange on the NMR timescale, modulating the observed $\delta(^{17}O)$ and C_Q values, while lattice or outer-

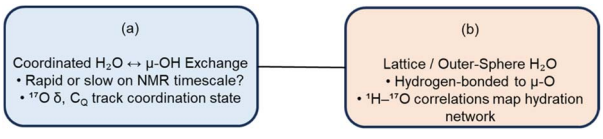

Fig. 13 Hydration motifs in the ^{17}O NMR view of polyoxometalates. (a) Coordinated water molecules undergo μ–OH exchange, with the exchange rate – rapid or slow on the NMR timescale – manifested in variations of $\delta(^{17}O)$ and quadrupolar coupling (C_Q), reflecting local coordination geometry. (b) Lattice or outer-sphere H_2O forms hydrogen bonds to μ–O sites, where ^{1}H–^{17}O correlation spectra trace extended hydration networks and distinguish structural *versus* dynamic water species.

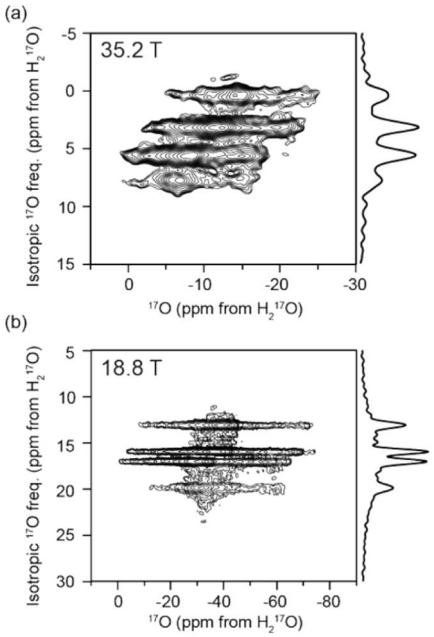

Fig. 14 ^{17}O 2D MQMAS NMR spectra of a hydrated crystalline sample of Lanthanum magnesium nitrate hydrate, $La_2Mg_3(NO_3)_{12}\cdot 24H_2{}^{17}O$, prepared from $H_2{}^{17}O$ showing the improvement in resolution at ultrahigh magnetic field: (a) 35.2 T ($\omega_0H/2\pi = 1500$ MHz) and (b) 18.8 T ($\omega_0H/2\pi = 800$ MHz). Four distinct water (H_2O) oxygen sites are resolved in each spectrum. The corresponding isotropic-dimension projections are shown on the right-hand side, illustrating reduced second-order quadrupolar broadening and enhanced site discrimination at 35.2 T relative to 18.8 T. Reprinted with permission from ref. 128. Copyright 2019, American Chemical Society.

sphere water interacts with bridging oxygens through hydrogen bonding. Proton-detected ^{1}H–^{17}O correlations thus provide a powerful means to map these hydration networks and distinguish between bound and outer-sphere environments.

Fig. 14 demonstrates how high-field and multidimensional ^{17}O NMR spectroscopy can resolve distinct classes of water molecules associated with hydrated oxo frameworks and POM salts. The representative 2D ^{17}O MQMAS spectra[128] distinguish three categories of oxygen sites: lattice, coordinated, and interstitial water, through variations in isotropic chemical shifts (δ_{iso}) and quadrupolar coupling constants (C_Q, η). These differences originate from the degree of hydrogen bonding and proximity to the inorganic cluster surface. Lattice water exhibits the smallest C_Q ($\approx$6–7 MHz) and moderate deshielding ($\delta_{iso} \approx$ 0–40 ppm), reflecting restricted rotational freedom and strong H-bonding to oxide anions. Coordinated water bound directly to metal centers displays broader line shapes and more deshielded δ_{iso} values ($\approx$50–150 ppm), indicative of partial covalent character and anisotropic EFGs. Interstitial or weakly bound water gives sharper resonances at higher fields and reduced C_Q, corresponding to fast dynamic averaging. The figure thus encapsulates how ^{17}O NMR quantifies hydration heterogeneity at an atomic level, which is an effect that is equally crucial in hydrated POM crystals, POM@MOF composites, and supported POM catalysts.[10] At ultrahigh fields ($\geq$28–35 T) and under fast MAS, ^{1}H-detected ^{1}H $\rightarrow$ ^{17}O HETCOR or D-RINEPT methods enhance sensitivity and allow for correlation of proton environments with specific oxygen sites, directly mapping hydrogen-bond networks and hydration shells.[50,129] In solution, analogous δ_{iso} shifts of solvent-derived ^{17}O signals track exchange between coordinated and bulk water, providing a dynamic complement to ^{31}P and ^{183}W probes that reflect the metal environment. These insights generally confirm that hydration layers around POMs strongly modulate both electronic and quadrupolar parameters, and that ^{17}O NMR uniquely captures this interplay between structure, dynamics, and local bonding.

4.1.3 Oxygen exchange with solvent water. Site-selective exchange between POM oxygens and solvent $H_2{}^{17}O$ has long been monitored by ^{17}O NMR to reveal which O classes are labile, and under what conditions (pH, Temperature, ionic strength). Early and subsequent solution studies on heteropolyanions (including V-containing Keggin/Dawson motifs) showed that different oxygen types exchange at distinct rates; exchange patterns depend on the anion composition and can be quantified by signal growth/decay in time-dependent ^{17}O spectra.[130] For Nb/Ta isopolyanions, time-series ^{17}O spectra directly

Table 6 Exchange-rate regimes on the ^{17}O NMR timescale – kinetic criteria (k_{ex} *versus* $|\Delta\omega|$), diagnostic observables (δ_{iso}, line-shape/coalescence, T_1/T_2), and recommended experiments (multi-field, variable-T line-shape, EXSY/HETCOR, DNP-assisted detection)

Exchange regime	Kinetic criterion (k_{ex} relative to $\Delta\omega$)	^{17}O observables	Useful experiments	Selected ref.
Slow	$k_{ex} \ll \lvert\Delta\omega\rvert$ (rad s^{-1}); separate sites	Distinct ^{17}O resonances for exchanging sites; linewidths set by T_2/quadrupolar effects; no coalescence	Static/multi-field lineshape; time-resolved isotopic incorporation; 2D EXSY	13, 19 and 133
Intermediate	$k_{ex} \sim \lvert\Delta\omega\rvert$; coalescence regime	Marked broadening; partial coalescence; temperature and field dependence diagnostic	Variable-T line-shape; multi-field; 2D EXSY/HETCOR to anchor assignments	19, 50 and 125
Fast	$k_{ex} \gg \lvert\Delta\omega\rvert$; motional averaging	Single averaged ^{17}O resonance; narrowed quadrupolar patterns; exchange impacts T_1/T_2	Relaxometry; multi-nuclear correlation; DNP-assisted detection at low enrichment	51–55

identified protonation sites and transient species during hydrolysis/condensation (*e.g.*, decaniobate ↔ hexaniobate), showcasing how exchange couples to acid–base speciation.[131]

In modern procedures, multi-field experiments separate chemical-shift from second-order quadrupolar contributions to extract reliable δ_{iso} and C_Q during exchange,[132] while DFT helps assign new resonances as transient μ–OH/μ–O environments form. In solids or immobilized POM composites, variable-temperature and ^{1}H-detected ^{17}O correlation experiments can distinguish static *vs.* dynamic hydration and detect exchange-broadened features.[125] Table 6 provides a practical approach for interpreting chemical exchange in ^{17}O NMR, classifying processes as slow ($k_{ex} \ll |\Delta\omega|$), intermediate ($k_{ex} \sim |\Delta\omega|$; coalescence regime), or fast ($k_{ex} \gg |\Delta\omega|$; motional averaging), where $\Delta\omega$ is the angular frequency separation between non-exchanging sites ($\Delta\omega = 2\pi\Delta\nu$). For quadrupolar ^{17}O, second-order broadening complicates simple line-shape intuition; accordingly, the table links each regime to concrete parameters, that is, discrete site resolution and quadrupolar-dominated widths (slow), pronounced broadening/coalescence with strong temperature and field dependence (intermediate), and single averaged resonances with exchange-modulated relaxation (fast). The recommended experiments are listed alongside, *i.e.* multi-field datasets ($|\Delta\omega| \propto B_0$ while second-order effects diminish with B_0) and variable-T Bloch–McConnell fits to extract k_{ex} and activation parameters; 2D EXSY to prove exchange connectivity; ^{1}H–^{17}O HETCOR to anchor assignments; and, where enrichment is limited, DNP-assisted detection. Together these guidelines enable consistent, site-resolved analysis of protonation, hydration, and O-atom exchange dynamics in POMs and related oxides.

4.2 Monitoring catalytic transformations

4.2.1 Peroxo formation and oxygen-atom transfer (OAT). Under oxidising conditions such as in the presence of H_2O_2, many POMs form peroxo adducts, typically mono-(η^2–O_2) or di-(μ–η^2:η^2–O_2) species, whose oxygen nuclei exhibit distinctly downfield ^{17}O chemical shifts and diagnostic quadrupolar coupling constants. These spectroscopic features allow ^{17}O NMR to differentiate mono- and di-peroxo intermediates, monitor their interconversion and protonation states, and thereby track critical steps in oxygen-atom-transfer (OAT) and electrophilic oxidation pathways.[123]

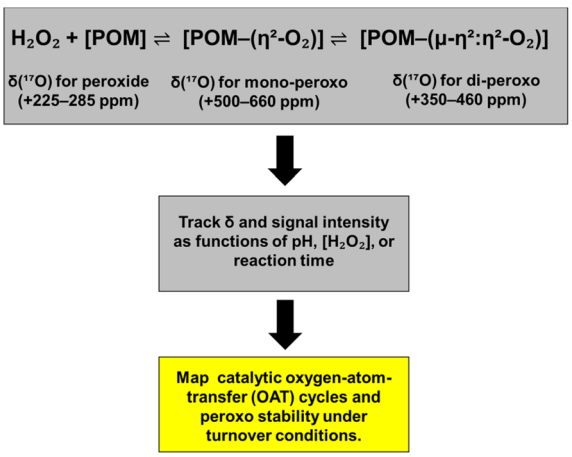

Fig. 15 Following peroxo speciation and oxygen-atom-transfer (OAT) processes in POMs by ^{17}O NMR spectroscopy.

Fig. 15 summarizes this sequence of peroxo speciation and its corresponding ^{17}O NMR signatures. Upon reaction of H_2O_2 with a POM, the free peroxide ($\delta(^{17}O) \approx$ +225–285 ppm) converts to mono-peroxo adducts ([POM–(η^2–O_2)], $\delta(^{17}O) \approx$ +500–660 ppm) and, under more oxidising or acidic conditions, to di-peroxo species ([POM–(μ–η^2:η^2–O_2)], $\delta(^{17}O) \approx$ +350–460 ppm). By tracking $\delta(^{17}O)$ shifts and signal intensities as functions of pH, [H_2O_2], and reaction time, one can map catalytic OAT cycles and assess peroxo stability under turnover conditions.

Solution-state ^{17}O NMR studies on peroxotungstates and peroxomolybdates have identified numerous transient and equilibrium species, establishing reproducible chemical-shift patterns across wide pH and peroxide-concentration ranges. This allows for confident assignments even in complex or kinetically trapped systems.[123,134] More broadly, correlations between ^{17}O observables (δ, C_Q, and EFG tensor parameters) and frontier orbital energies offer predictive insights into peroxide activation and reactivity trends, providing a quantitative link between electronic structure and catalytic behaviour in POM-mediated oxidation chemistry.[122]

Furthermore, Fig. 16 presents the representative ^{17}O NMR spectra and structural assignments of mono- and diperoxo peroxotungstate species that form in aqueous solution over a wide range of pH and peroxide concentrations. The spectra clearly resolve distinct oxygen environments corresponding to monomeric $[WO(OH)(O_2)_2]^-$ (WX_2) and dimeric $[W_2O_3(O_2)_4]^{2-}$ (W_2X_4), which dominate when the peroxide: metal ratio >2. Both species exhibit strongly downfield terminal-oxygen resonances ($\delta \approx$ 655–657 ppm) and bridging-oxygen signals near 245 ppm, consistent with highly deshielded η^2–O_2 ligands relative to M=O groups.[122,123] The proportional deshielding (W/Mo shift ratio ≈0.79 ± 0.02) confirms structural homology to the corresponding molybdenum peroxo analogues.

The mono-peroxo monomer $[WO(OH)(O_2)_2]^-$ displays an asymmetric electronic field around each O_2 unit, reflected in the inequivalent oxo and hydroxyl resonances ($\delta \approx$ 655 ppm and 91 ppm), while the diperoxo dimer $[W_2O_3(O_2)_4]^{2-}$ shows a more averaged environment and slightly reduced quadrupolar coupling, indicating more delocalized electron density across the μ–η^2:η^2–O_2 bridge. These findings quantitatively link δ_{iso} and C_Q values to bonding symmetry and M–O covalency.

Complementary spectra at lower peroxide ratios (H_2O_2/W ≈ 0.5–2) reveal additional peroxo-oligomers – $[W_4O_{12}(O_2)_2]^{4-}$ and $[W_7O_{22}(O_2)_2]^{6-}$ – whose terminal oxygen shifts ($\delta \approx$ 621–648 ppm) remain systematically downfield from those of non-peroxidised tungstates. Taking comprehensively, these data confirm that formation of peroxo ligands generates large positive δ shifts and altered C_Q values, diagnostic of π back-donation from W 5d to O_2 π* orbitals. Such back-bonding narrows the HOMO–LUMO gap and enhances oxygen-atom-transfer (OAT) reactivity,[122] explaining the strong correlation

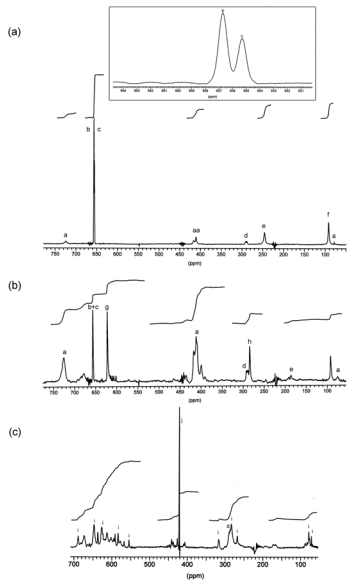

Fig. 16 Solution-state ^{17}O NMR spectra. (a) 0.3 mol dm^3 aqueous tungstate, pH 4.06, $[H_2O_2]/[W] = 2.0$. a = probable peroxo-Keggin anion; b = $[W_2O_3(O_2)_4]^{2-}$, (terminal O); c = $[WO(OH)(O_2)_2]^-$ (terminal O); d = $[ClO_4]^-$; e = $[W_2O_3(O_2)_4]^{2-}$, bridging O; f = $[WO(OH)(O_2)_2]^-$ (OH). Inset: expansion of peaks b and c. (b) as (a) but pH 3.49, $[H_2O_2]/[W] = 1.0$, g = $[W_4O_{12}(O_2)_2]^{4-}$ (terminal O); h = $[W_4O_{12}(O_2)_2]^{4-}$ (bridging O). A second, more minor Keggin-like species is also seen. (c) as (a) but pH 7.46, $[H_2O_2]/[W] = 0.5$, i = peaks arising from $[W_7O_{23}(O_2)]^{6-}$ and $[W_7O_{22}(O_2)_2]^{6-}$; j = $[WO_4]^{2-}$. Reproduced from ref. 123. Copyright 2004, Royal Society of Chemistry.

between ^{17}O chemical shifts and catalytic activity in electrophilic epoxidation and oxidation processes. Hence, ^{17}O NMR provides a direct spectroscopic fingerprint of peroxo coordination, protonation, and redox activation. δ and C_Q together distinguish mono-*versus* diperoxo species, track interconversion and protonation equilibria, and quantify electronic activation that underpins OAT reactivity in polyoxotungstate systems.[122,123,134]

4.2.2 Proton-coupled electron transfer (PCET), reduction, and oxygen defects. Catalytic redox events redistribute electron density and sometimes generate oxygen-atom vacancies (*e.g.*, in polyoxovanadates). ^{17}O NMR reports these changes through systematic δ shifts and altered quadrupolar parameters at oxygens adjacent to reduced or substituted metals; when oxygen vacancies form, signals associated with the eliminated/perturbed sites vanish or move, providing structural constraints complementary to UV-vis/EPR and $^{51}V/^{183}W$ NMR.[14] As illustrated in Fig. 17–19, recent work on hexavanadate assemblies, for instance, linked oxygen-atom vacancy formation to PCET pathways relevant to (electro)catalytic function.[135–137] The figures collectively depict the interplay between redox activity, structural reorganisation, and oxygen-vacancy generation in hexavanadate polyoxovanadate (POV-alkoxide) clusters. Cyclic voltammetry data (Fig. 17) show that each reduction step corresponds to sequential electron addition coupled to proton transfer, indicating that the reduction is accompanied by oxygen-atom loss from bridging sites. The resulting mono- and di-vacant species (Fig. 18) reveal how these redox events redistribute electron density over the remaining V–O framework, converting localized V^{5+} centers to mixed-valent V^{4+}/V^{5+} arrays. ^{17}O NMR and complementary spectroscopies (UV-vis, EPR, ^{51}V) detect these changes through systematic chemical-shift and quadrupolar-parameter variations at oxygens adjacent to reduced vanadium centers, and by loss or broadening of signals from sites where vacancies form. Such behaviour reflects both electronic delocalization and structural asymmetry around the newly reduced core. The mechanistic scheme (Fig. 19) ties these observations to a proton-coupled electron-transfer (PCET) pathway, wherein sequential redox–protonation cycles generate and stabilise oxygen vacancies, mimicking catalytic turnover in polyoxovanadate and metal-oxide catalysts. These integrated results demonstrate that ^{17}O NMR offers a direct, site-resolved probe of oxygen-vacancy chemistry. The shifts in $\delta(^{17}O)$ and C_Q track redox-driven lattice reorganisation, while disappearance of resonances identifies vacancy creation. Coupled with electrochemical and computational analyses, the three figures illustrate how structural, electronic, and spectroscopic signatures converge to elucidate redox-active oxygen dynamics fundamental to (electro)catalytic function.[13,138]

4.2.3 Exchange with solvent water during turnover. In oxidation catalysis mediated by heteropolytungstates, molybdates, vanadates or mixed-addenda systems, ^{17}O NMR can directly follow both the incorporation and subsequent washout of label from $H_2{}^{17}O$ into the POM lattice or into peroxo ligands,

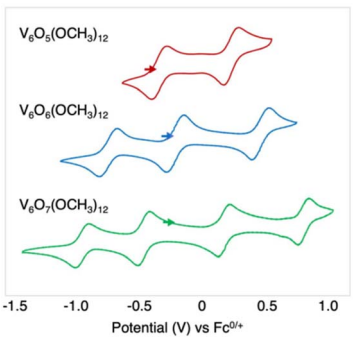

Fig. 17 Cyclic voltammograms of fully-oxygenated (bottom, green), mono-vacant (middle, blue), and di-vacant (top, red) POV-alkoxide clusters. CV collected in dichloromethane with 0.1 M[^{n}Bu$_4$N][PF$_6$] as supporting electrolye. Reproduced from ref. 138. Copyright 2020, Royal Society of Chemistry.

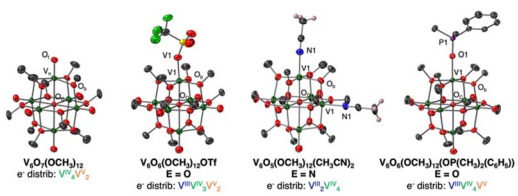

Fig. 18 Molecular structures of complexes $[V_6O_7(OCH_3)_{12}]^{1-}$, and $[V_6O_6(OCH_3)_{12}]OTf$, $[V_6O_5(OCH_3)_{12}]$, and with 30% probability ellipsoids. Hydrogen atoms, counter ions and solvent molecules have been omitted for clarity. Key: O, red; V, dark green; C, grey; S, yellow; F, light green; N, blue; P, purple; H, pink. Reproduced from ref. 138. Copyright 2020, Royal Society of Chemistry.

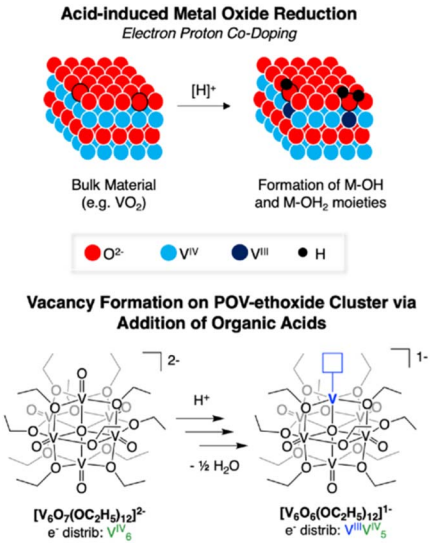

Fig. 19 Schematic representation of proton-induced activation on a metal oxide surface (top) and the comparable reactivity observed in POV-alkoxide clusters (bottom). Reproduced from ref. 138. Copyright 2020, Royal Society of Chemistry.

thereby distinguishing mechanisms in which lattice oxygen participates in oxygen-atom transfer (OAT) from those where the oxidant is the exclusive O-atom donor.[123,134] Early ^{17}O-exchange work on V-containing heteropolyanions revealed pronounced site-dependent exchange with water, and modern speciation analysis together with DFT now links those exchange patterns to detailed proposals for POM-mediated OAT and water–activation cycles.[130]

Fig. 20 presents the structural frameworks of decavanadate and bicapped-Keggin heteropolyphosphovanadate, highlighting spatially distinct oxygen environments that govern isotopic exchange behaviour (polar "caps" *vs.* equatorial sites). In $[HPV_{14}O_{42}]^{8-}$, the ^{17}O spectrum resolves these non-equivalent oxygen classes, enabling site-specific tracking of exchange with $H_2{}^{17}O$. Fig. 21 and 22 together show that capping oxygens [O_{cap}, $O_{E(cap)}$] exchange rapidly across a broad pH range, whereas equatorial oxygens [$O_{P(1,2)}$, $O_{T(1,2)}$] are comparatively inert, yielding a quantitative map of water–framework exchange and lattice lability. The geometric correlation in

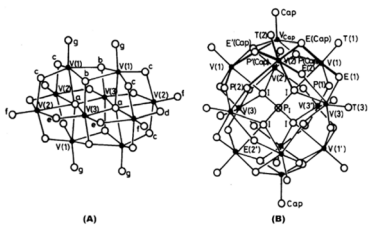

Fig. 20 Representative structures of decavanadate, $[V_{10}O_{28}]^{6-}$ and bicapped-Keggin heteropolyphospho-vanadate, $[HPV_{14}O_{42}]^{8-}$ showing inequivalent oxygen sites relevant to ^{17}O–$H_2{}^{17}O$ exchange and peroxo labelling studies. Reproduced from ref. 140. Copyright 1985, Royal Society of Chemistry.

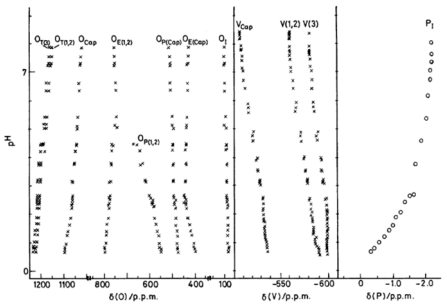

Fig. 21 pH-dependent chemical-shift (^{17}O, ^{51}V and ^{31}P) trends for heteropolyphosphovanadate highlighting proton-linked distortions and site-specific exchange. Reprinted, with permission from ref. 140. Copyright 1985, Royal Society of Chemistry.

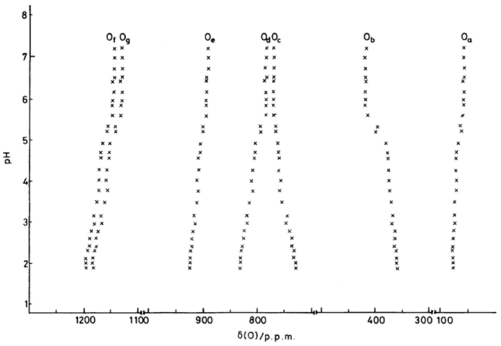

Fig. 22 pH-dependent ^{17}O chemical-shift trends for decavanadate highlighting proton-linked distortions and site-specific exchange. Reproduced from ref. 140. Copyright 1985, Royal Society of Chemistry.

Fig. 23, linking $\delta(^{17}O)$ to the M–O–M angle, demonstrates the exquisite sensitivity of ^{17}O shifts to bond-angle distortions at bridging oxygens. These distortions give information on structural strain and protonation-driven reorganisation, providing an accurate probe of local geometry and bonding. Fig. 24 then quantifies these trends by plotting the pH-dependent pseudo-first-order rate constants for ^{17}O exchange between the heteropolyphosphovanadate framework and solvent $H_2{}^{16}O$. It establishes a clear ordering of site lability: O_{cap} is consistently the most labile across the pH range, whereas $O_{E(1,2)}$ and $O_{P(1,2)}$ accelerate markedly under acidic conditions (pH < 5), and $O_{T(3)}$ retains residual stability. The kinetic profile thus reveals a switch from relatively slow exchange near neutral pH (with measurable stabilisation above ~6.5) to global labilization at low pH, capturing the electrostatic and protonation control of oxygen mobility within the anion.

These principles are integrated in Fig. 25 under catalytic conditions, illustrating incorporation and washout of ^{17}O label in a Keggin-type POM, the lattice-versus-oxidant oxygen sources operative in OAT, and the pH-dependent exchange kinetics. In practice, combining the experimental ^{17}O observables with DFT-predicted $\delta(^{17}O)$ helps determine whether OAT steps draw from the lattice or from peroxo intermediates. These results (Fig. 20–25) demonstrate that ^{17}O NMR acts as a direct

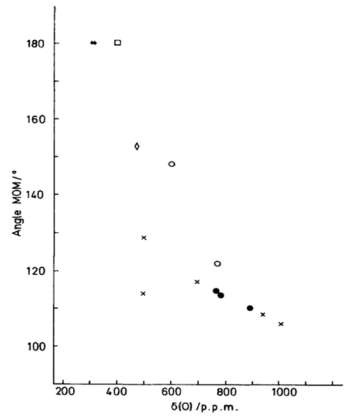

Fig. 23 Inverse correlation between ^{17}O chemical shift and M–O–M angle showing sensitivity of ^{17}O NMR to geometric distortions at bridging oxygens. Points: ●, decavanadate (O_c, O_d, and O_e); ○, heteropolyphosphovanadate [$O_{E(1,2)}$ and $O_{p(1,2)}$]; x, $[Mo_6O_{19}]^{2-}$ and $[Mo_7O_{24}]^{6-}$ (reassigned to fit published integrals); □, $[V_2O_7]^{4-}$; *, $[Mo_2O_7]^{2-}$; and ◇, $[HV_4O_{12}]^{3-}$. Reproduced from ref. 140. Copyright 1985, Royal Society of Chemistry.

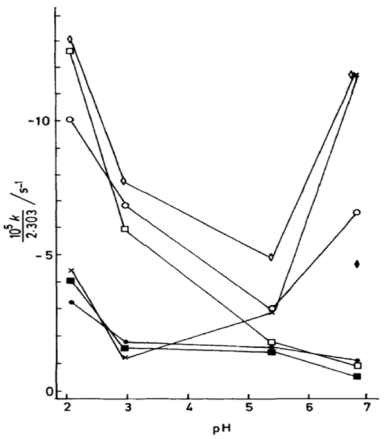

Fig. 24 pH dependence of ^{17}O–$H_2{}^{16}O$ exchange in $[HPV_{14}O_{42}]^{8-}$ indicating differential lability of terminal, bridging, and capping oxygens – mechanistic analogues for OAT steps in POM oxidation catalysis. ◇, $O_{P(1,2)}$; □, $O_{P(Cap)}$; ○, $O_{T(1,2)}$; x, $O_{E(1,2)}$; ■, $O_{T(3)}$; ●, $O_{E(Cap)}$; ◆, O_{Cap}. Reproduced from ref. 140. Copyright 1985, Royal Society of Chemistry.

spectroscopic readout of oxygen flow through POM frameworks, cleanly separating lattice-involved OAT from oxidant-supplied pathways. The observed pH-dependent exchange kinetics provide the catalytic context in which ^{17}O information are most diagnostic, and they align with mechanistic assignments for mixed-addenda W/Mo/V systems that couple isotopic labelling, high-field NMR, and computation.[10,139]

4.2.4 *Operando*-style ^{17}O NMR workflow for POM catalysis.

The effective deployment of ^{17}O NMR in POM catalysis relies on an integrated, *operando* workflow that couples isotope labelling, speciation control, advanced spectral acquisition, and theory-assisted analysis to deliver site-resolved mechanistic insight into oxygen-atom-transfer (OAT) and proton-coupled electron-transfer (PCET) processes (Fig. 26). The workflow begins with a targeted isotope-introduction strategy (Fig. 26a), in which $H_2{}^{17}O$, ^{17}O-labelled peroxides, or site-selective enrichment schemes are used to incorporate ^{17}O into terminal or bridging oxygen sites within the POM framework or reactive intermediates. *Operando* control of reaction and speciation parameters (Fig. 26b), including pH, redox state, temperature, and gas atmosphere ensures that the catalytically relevant POM forms are maintained during measurement. Subsequently, time-resolved ^{17}O NMR acquisition (Fig. 26c), enabled by high magnetic fields, fast magic-angle spinning (MAS), and heteronuclear 1H → ^{17}O detection, captures the evolution of oxygen environments as a function of reaction time or conversion. Spectral assignment (Fig. 26d) is achieved by correlating experimental ^{17}O chemical shifts and quadrupolar parameters with GIPAW-DFT predictions, often supported by multi-nuclear and multi-field datasets that link structure and spectrum quantitatively. Where sensitivity limits arise, signal-enhancement strategies such as dynamic nuclear polarisation (DNP) or surface-selective labelling (Fig. 26e) extend the accessible regime to low-enrichment samples and transient intermediates, enabling iterative *operando* measurements. Ultimately, the integration of isotope dynamics, spectral evolution, and DFT-validated assignments yields a mechanistic read-out (Fig. 26f) of key catalytic processes, including oxygen exchange kinetics, peroxo formation and cleavage, and coupled OAT/PCET pathways. Collectively, this workflow transforms ^{17}O NMR from a predominantly static structural probe into a time-resolved, site-specific *operando* sensor, an approach that is gaining increasing traction across POM and nanoporous catalyst systems.[87,91,141–145]

Recent *operando* and time-resolved ^{17}O NMR "tracking" studies in catalytic materials provide concrete templates that can be adapted to POM-based oxidation and electrocatalysis. For example, advances in high-temperature/high-pressure *operando* MAS rotor technology (including check-valve and sealed-rotor designs) have enabled realistic gas/liquid atmospheres, controlled temperature/pressure, and continuous-flow

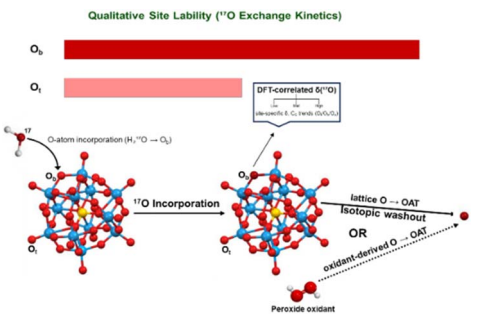

Fig. 25 Isotopic labelling and O-atom transfer in a Keggin-type POM. $H_2{}^{17}O$ exchanges at a bridging O_b site (O-atom incorporation), while OAT proceeds *via* lattice- or oxidant-derived pathways (solid *vs.* dashed). Overlay of relative pseudo-first-order rate constants (qualitative). Thicker and darker bars denote higher oxygen-site lability. O_b is the most exchange-active across pH, and the rigid O_t is the least. An inset shows DFT-correlated $\delta(^{17}O)$ for site assignment.

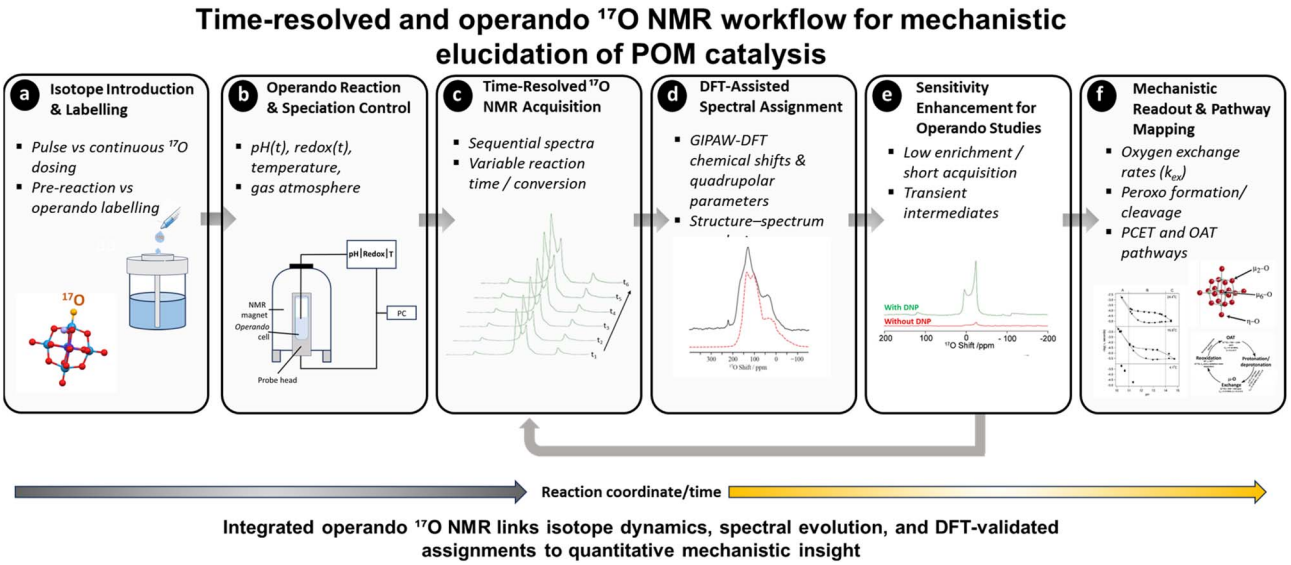

Fig. 26 Time-resolved and *operando* ^{17}O NMR workflow for mechanistic elucidation of oxygen chemistry in polyoxometalate (POM) catalysis. (a) Isotope introduction and labelling, illustrating pulse *versus* continuous $H_2{}^{17}O$ dosing and pre-reaction *versus operando* ^{17}O incorporation into distinct POM oxygen sites. (b) *Operando* reaction and speciation control, where pH(t), redox state, temperature, and gas atmosphere are regulated within an *operando* NMR-compatible reaction cell. (c) Time-resolved ^{17}O NMR acquisition, showing sequential spectra collected as a function of reaction time or conversion, enabling tracking of evolving oxygen environments. (d) DFT-assisted spectral assignment, where experimental ^{17}O NMR spectra are correlated with GIPAW-DFT-calculated chemical shifts and quadrupolar parameters to achieve site-resolved oxygen assignments. (e) Sensitivity enhancement for *operando* studies, exemplified by dynamic nuclear polarisation (DNP), enabling short acquisition times, low isotope enrichment, and detection of transient intermediates, with feedback to time-resolved acquisition. (f) Mechanistic readout and pathway mapping, integrating isotope dynamics, spectral evolution, and computational validation to extract quantitative oxygen-exchange rates (k_{ex}), peroxo formation/cleavage steps, and PCET/OAT pathways. The horizontal axis represents the reaction coordinate or time, emphasising the *operando* and iterative nature of the workflow. (a) Is an original schematic created for this work. (b) Is adapted from S. Jovanovic, P. P. M. Schleker, M. Streun, S. Merz, P. Jakes, M. Schatz, R.-A. Eichel and J. Granwehr, Magn. Reson., 2021, 2, 265–280, https://doi.org/10.5194/mr-2-265-2021. © Author(s) 2021. Distributed under the Creative Commons Attribution 4.0 Licence (CC BY 4.0).[146] Original figure used under the Creative Commons Attribution 4.0 International Licence (CC-BY 4.0) and modified for presentation in this work. (c) and (e) are adapted from ref. 47. Copyright 2017, Royal Society of Chemistry. (d) Is adapted from R. Dervişoğlu, D. S. Middlemiss, F. Blanc, Y.-L. Lee, D. Morgan and C. P. Grey, *Chem. Mater.*, 2015, 27, (3861-3873), https://doi.org/10.1021/acs.chemmater.5b00328. Copyright 2015, American Chemical Society. Original work licensed under the Creative Commons Attribution 4.0 International Licence (CC BY 4.0).[147] (f) is adapted with permission from ref. 41. Copyright 2006, American Chemical Society.

operation – capabilities that are directly relevant to monitoring oxygen-site evolution during POM-mediated oxidation or POM-derived catalyst activation.[148]

In parallel, *operando* electrochemical NMR approaches have demonstrated real-time detection and quantification of oxygen-containing species using ^{17}O NMR under working electrocatalytic conditions, highlighting how isotope tracking can be integrated with electrochemistry to follow reaction pathways and oxygen incorporation *in situ*.[143]

Beyond hardware development, isotopic oxygen-exchange tracking has been applied to working oxide catalysts to quantify oxygen incorporation, mobility, and reactivity under *operando* or quasi-*operando* conditions. For example, ^{17}O solid-state NMR studies of cerium dioxide (CeO_2) using $H_2{}^{17}O$ or $^{17}O_2$ labelling at elevated temperatures have directly distinguished lattice oxygen from surface hydroxyl and adsorbed oxygen species, revealing rapid lattice–surface exchange and identifying oxygen mobility as a key descriptor of redox and catalytic behaviour in ceria-based catalysts.[67] Similarly, time-resolved ^{17}O NMR investigations of TiO_2 and related transition-metal oxides under hydrated or oxidative conditions have tracked the formation and evolution of surface hydroxyl, peroxo-like, and exchangeable oxygen species, with spectral deconvolution and DFT/GIPAW analysis enabling assignment of distinct oxygen environments and exchange pathways.[93,149,150]

These studies exemplify a transferable *operando* workflow: controlled ^{17}O label introduction, monitoring spectral evolution as a function of time and reaction conditions, and DFT-supported assignment. This approach can be directly applied to POM–oxide composites and supported POM catalysts, where oxygen-atom transfer, peroxo/oxo intermediate formation, and framework–solvent exchange are central to catalytic and electrocatalytic mechanisms. Table 7 summarises representative *operando* and time-resolved ^{17}O NMR tracking platforms, the oxygen species and processes they probe, the mechanistic insights they deliver, and how these established workflows can be directly translated to polyoxometalate (POM) systems, thereby providing practical guidance for designing *operando* ^{17}O NMR studies in POM catalysis and materials chemistry.

While truly *operando* ^{17}O MAS NMR studies focused explicitly on intact POM frameworks remain comparatively limited, the rapid maturation of *operando* rotor and cell technologies,

Table 7 Representative *operando*/time-resolved ^{17}O NMR tracking paradigms and transferable relevance to POM systems

Operando platform	What is tracked	What is learned	Transferable relevance to POM systems	Ref.
HT/HP sealed MAS rotor (gas/vapour atmosphere)	^{17}O incorporation/exchange, lattice *vs.* surface oxygen identities	Oxygen mobility; lattice-surface exchange pathways; facet-specific oxygen environments	Tracking oxygen atom transfer (OAT) in POM oxidation catalysis; mapping exchange between POM frameworks and reactants	20
Continuous-flow MAS NMR	Time-dependent evolution of labelled oxygen species	Kinetics of oxygen exchange and transformation; identification of transient oxygen species	*Operando* monitoring of POM-mediated oxidation in flow reactors; distinguishing framework-derived *vs.* solvent oxygen	—
Operando electrochemical NMR cell	^{17}O-labelled electrolyte oxygen and surface oxygen intermediates	Role of oxygen species in electrochemical reactions	Studying POM electrocatalysts for water oxidation/O_2 evolution; probing oxygen participation at POM–electrode interfaces	—
Quasi-*operando* variable temperature/atmosphere	Reversible *vs.* irreversible exchange; hydration dependent environments	Activation pathways and dynamic restructuring	Mapping protonation, hydration effects in POM acids; identifying oxygen sites active before catalysis	20
Supported oxides/POM-oxide hybrids	Interface oxygen exchange/communication	Interfacial exchange kinetics; support effects on oxygen speciation	Understanding oxygen communication between POMs and oxide supports; design of supported POM catalysts	151
DFT-assisted *operando* analysis	Assignment of overlapping ^{17}O resonances	Structure–reactivity relationships; transient oxygen species	Predictive interpretation of spectral changes in POM *operando* experiments	20

together with isotope-tracking demonstrations in closely related catalytic oxides, now makes targeted translation to POM systems increasingly feasible. This is particularly relevant for supported POM catalysts, POM–oxide hybrids, and electrocatalytic environments, where oxygen exchange, peroxo/oxo intermediate formation, and lattice–surface communication are mechanistically decisive.[148] By combining selective ^{17}O labelling with multi-field and fast-MAS measurements, two-dimensional ^{1}H–^{17}O correlation experiments, exchange-sensitive NMR methods, and DFT-assisted analysis, ^{17}O NMR can deliver time- and site-resolved fingerprints of protonation, hydration, oxygen exchange, peroxo formation, and oxygen-atom transfer (OAT). Collectively, these capabilities extend ^{17}O NMR beyond static structural characterisation, enabling *operando* mechanistic mapping of POM structure–reactivity relationships under realistic working conditions.

5. Integration with computational methods

Computational chemistry, especially density functional theory (DFT), has become indispensable in interpreting and predicting ^{17}O NMR parameters in POMs. Calculated shielding and electric-field–gradient (EFG) tensors complement experiment by enabling site-specific assignments, quantifying substitution and protonation effects, and bridging structure with reactivity under realistic (solvated, dynamic) conditions. The most common approaches are (i) cluster calculations using GIAO-type formalisms for molecular models, and (ii) periodic plane-wave calculations using the GIPAW method, extended to ultrasoft pseudopotentials and, where relevant, relativistic Hamiltonians. These tools underpin modern "NMR crystallography" for POMs.[1,19,62]

5.1 DFT/NMR chemical shift predictions

5.1.1 Protocols and best practices. For discrete POM clusters, GIAO DFT with carefully chosen functionals and basis sets (often TZP/TZ2P on O and the addenda metals) is standard. Systematic benchmarking shows that hybrid functionals frequently improve absolute ^{17}O shift predictions for bridging sites, while pure GGAs often perform well for terminal oxo sites. Linear scaling against experiment further tightens accuracy. For periodic models (*e.g.*, extended solids, framework-embedded POMs), GIPAW is the method of choice and now robust with ultrasoft PAW libraries.[19,97] For heavy addenda (W, Mo, V, Nb, Ta), scalar-relativistic and, where needed, spin–orbit effects should be included (*e.g.*, ZORA/X2C), as neighbouring heavy atoms can measurably perturb ^{17}O shielding.[15,152]

5.1.2 From tensors to observables. DFT yields the full shielding tensor (σ) and the EFG tensor, which map to the isotropic shift (δ_{iso}) *via* $\delta = a\cdot\sigma_{ref} - \sigma + b$ (calibrated to a reference set), and to the quadrupolar coupling (C_Q) and asymmetry (η), enabling direct comparison to MAS, MQMAS/STMAS, and static spectra. Recent "EFG–to–NMR" best-practice guides and high-throughput databases have improved reliability and transferability across chemistries.[153–155]

5.1.3 Dynamics, solvation, and temperature. Static single-point calculations can misrepresent solution spectra when fluxionality, hydrogen bonding, or hydration dominate. *Ab initio* molecular dynamics (aiMD) and ensemble averaging (*e.g.*, on AIMD trajectories or implicit/explicit solvent clusters) capture motionally averaged ^{17}O shifts and quadrupolar relaxation, enabling quantitative comparison at experimental temperatures and ionic strengths.[154–156]

5.1.4 Machine learning (ML). ML models trained on DFT or experimental datasets can accelerate screening and provide uncertainty estimates. Although most developments target

Table 8 DFT-assisted ^{17}O NMR in POM chemistry – representative systems, experimental observables (δ_{iso}, C_Q, η; MAS/MQMAS/HETCOR), computational protocols (cluster GIAO, periodic GIPAW, AIMD; hybrids/TZP–TZ2P; PAW/ultrasoft; relativistic corrections), and the resulting structural or mechanistic insights

System (representative)	Experimental ^{17}O observation	DFT protocol (illustrative)	Key computational insight	Ref.
Keggin $[PW_{12}O_{40}]^{3-}$/ heteroatom-substituted	Overlapping O_t/O_b signals; subtle shifts upon M-substitution	Cluster GIAO; hybrid (*e.g.*, PBE0), TZP/TZ2P; linear calibration	Terminal-oxo δ indicates M–O covalency; hybrids improve O_b accuracy	13
Dawson $[P_2W_{18}O_{62}]^{6-}$	Multiple μ_2-bridges unresolved	Cluster GIAO; OPBE/PBE (NMR//OPT); regression	Fingerprints for internal *vs.* belt oxygens; guides isomer assignment	108
Lindqvist $[M_6O_{19}]^{n-}$ (M = Nb, Ta)	Protonation seen at μ_2–O_b	Cluster GIAO (+explicit H_2O)	Locates preferred protonation sites; cation pairing effects	105
Peroxotungstates	Distinct peroxo/oxo ^{17}O resonances; activity trends	Cluster DFT with relativistic corrections	^{17}O δ/C_Q correlate with peroxo activation; identifies active oxidant	123
Actinyl oxo complexes (uranyl carbonates)	Strong T-dependence of ^{17}O relaxation	AIMD + shielding/EFG averaging	Quantifies solvation/dynamics; links relaxation to exchange	156
Microporous hosts with incorporated POMs	Convolution of framework *vs.* cluster ^{17}O signals	Periodic GIPAW (ultrasoft)	Assigns framework/cluster oxygens; detects host–guest H-bonding	19
General solids	Need for reliable PAW sets for d-elements	GIPAW with curated PAWs	Improved accuracy for W/Mo/Nb systems	97

organic solids, recent work extends to general solids and quadrupolar tensors, suggesting opportunities for rapid prediction of ^{17}O shifts in large POM libraries.[157–159]

5.2 Synergy between experiment and theory

5.2.1 Site assignment and isomer discrimination. In Lindqvisit, Keggin, and Dawson families, experimental ^{17}O resonances for terminal (O_t), edge-bridging (O_b), and internal μ_3–O sites often overlap. DFT-computed $\delta(^{17}O)$ and C_Q disentangle these by delivering site-resolved fingerprints, including the effects of heteroatom substitution (*e.g.*, Ti^{IV}, V^{V}, Nb^{V}) and vacancy/lacunary formation. Benchmark studies establish transferable linear calibrations and show that terminal-oxo shifts indicate metal–oxo bond covalency.[13,15]

5.2.2 Protonation, hydration, and counter-cations. Combined ^{17}O NMR/DFT has mapped where protons reside in niobate clusters (*e.g.*, doubly-bridging O sites in $\{Nb_6O_{19}\}^{8-}$) and how hydration/cation pairing modulate local fields and exchange rates – information difficult to access crystallographically.[105]

5.2.3 Reactive intermediates and mechanisms. For peroxotungstates and related oxidants, ^{17}O shifts and C_Q values correlate with frontier–orbital interactions that govern oxygen-transfer activity. DFT rationalizes these trends and helps identify the "true" oxidising species in catalytic cycles. In actinyl POMs and related oxo complexes, AIMD-averaged ^{17}O parameters quantify solvation effects and quadrupolar relaxation, linking measurable NMR timescales to ligand exchange.[123]

5.2.4 NMR crystallography of porous/embedded systems. For POMs in microporous hosts or hybrid architectures, ^{17}O NMR combined with GIPAW facilitates assignment of framework *vs.* cluster oxygens, probing host–guest interactions and acid sites under working conditions, which are often inaccessible to diffraction alone.[19,127]

Table 8 highlights how computation approach streamlines interpretation of ^{17}O spectra across representative POM systems. In each case, calculated shieldings and EFGs convert congested experimental data into site-resolved information, clarify isomerism or substitution patterns, and show protonation/exchange pathways relevant to catalysis. Where necessary, periodic models, relativistic effects, or modest AIMD sampling are used to capture framework, heavy-atom, and solvation influences. The common thread is that pairing DFT with ^{17}O parameters (δ_{iso}, C_Q, η) reduces assignment challenges and provide chemical insights into observed spectral trends.

5.3 A concise practical "recipe" for incorporating computation model

(1) Choose model: cluster (GIAO) for discrete ions/solution; periodic (GIPAW) for solids or host–guest.

(2) Include solvation/dynamics if spectra are temperature- or pH-dependent (PCM + explicit waters or AIMD).

(3) Use scalar-relativistic (and SOC when needed) for heavy addenda.

(4) Calibrate $\delta(^{17}O)$ *via* linear regression to ^{17}O references that match your chemical space; report σ tensors, C_Q, and η_Q with uncertainties.

(5) Validate assignments with complementary nuclei ($^{31}P/^{51}V/^{183}W$) and 2D ^{1}H–^{17}O correlations where available; iterate with experiment.

Pairing experiment with computation: GIAO (cluster) and GIPAW (periodic) DFT, with appropriate relativistic treatments and, where needed, AIMD/solvation and ML proxy models, turns raw ^{17}O observables (δ_{iso}, C_Q, η) into site-specific assignments and mechanistic insight, enabling the disentanglement of $O_t/O_b/O_i$ overlaps, locate protonation/hydration, benchmark substitution and isomerism, and identify catalytically relevant peroxo/OAT pathways with quantitative confidence.

6 Artificial intelligence (AI) and data-driven approaches in ^{17}O NMR of polyoxometalates

AI and ML are reshaping how ^{17}O NMR informs POM structure and catalysis, from predictive modelling of NMR parameters to automated spectral analysis, accelerated computation, and FAIR data infrastructure.

6.1 Predictive models of NMR observables (δ_{iso}, C_Q, η)

As noted earlier, modern ML models learn structure–spectrum relationships from large, computed-and/or experimental corpora, enabling fast, DFT-level predictions of shielding tensors and electric-field gradients (EFGs) central to quadrupolar nuclei like ^{17}O. Early "local-environment" ML set the stage for solid-state chemical shifts in molecular solids, now extended by GNNs and equivariant networks that directly learn tensor quantities (shielding anisotropy, EFG) and even static 1D spectra. These frameworks are well-suited to W/Mo/V–O networks in POMs and can be fine-tuned to capture site classes (O_t, O_b, O_c) and M–O–M angle effects that dominate ^{17}O signatures.[157,159–161]

6.2 Active-learning loops and inverse design

Coupling ML predictors with DFT/GIPAW in active-learning cycles allows rapid triage of candidate POM structures. Models propose structures with target ^{17}O windows ($\delta/C_Q/\eta$), while new experimental assignments update the model, reducing expensive enrichment campaigns. Recent 3D GNNs that fuse atomic features with DFT-derived tensors exemplify these hybrid physics–ML approaches, accelerating assignment and hypothesis testing in mixed-addenda systems.[162]

6.3 Accelerated computation of NMR parameters

ML surrogates can replace or pre-screen costly first-principles shielding calculations, delivering near-DFT accuracy at a fraction of the time. This is useful for *operando* sequences where rapid turnaround matters. Such acceleration supports broader speciation sweeps (pH/ionic strength/counter-ion) and sensitivity analyses that would be impractical with DFT alone.[163]

6.4 AI-assisted spectral deconvolution and reconstruction

For complex or low-S/N datasets, which is typical for quadrupolar ^{17}O-Bayesian and deep-learning approaches assist lineshape deconvolution, component separation, and reconstruction from undersampled data. These tools help resolve overlapping ^{17}O manifolds and quantify label in/label out kinetics under varied exchange regimes (slow–intermediate–fast).[164,165]

By integrating machine learning with ^{17}O NMR and DFT, AI now enables rapid, data-driven prediction, deconvolution, and design – linking structural motifs to δ_{iso}, C_Q, and η with near-DFT accuracy, accelerating enrichment and analysis cycles, and paving the way for automated, inverse-designed, and FAIR-compliant ^{17}O-POM spectroscopy that unites experimental insight with digital intelligence.

7. Current challenges and emerging opportunities in ^{17}O NMR of polyoxometalates

Despite major progress in hardware, pulse sequences, and labelling chemistry, several bottlenecks still limit the routine use of ^{17}O NMR for POMs. Chief among them are (i) the cost and protocol complexity of isotopic enrichment; (ii) spectral congestion from overlapping quadrupolar-broadened signals that often demands ultra-high fields and advanced correlation methods; and (iii) the need for truly *in situ/operando* experiments that maintain catalytic conditions while preserving spectral quality. Encouragingly, innovations in labelling (including room-temperature or mechanochemical routes), sensitivity (cryogenic probes, DNP), and resolution (ultrafast MAS at 80–160 kHz, 28–35.2 T magnets) are transforming what is feasible, while emerging application domains including bio-inorganic POM hybrids and energy technologies are poised to benefit directly from site-specific oxygen output.[19,20,64]

7.1 Isotopic labelling strategies[166]

Traditional enrichment with $H_2{}^{17}O/H_2{}^{17}O_2$ or $^{17}O_2$ at elevated temperature can be effective but remains costly and labour-intensive, especially for sensitive POM frameworks. Recent work offers gentler, cheaper, and often surface-selective alternatives:

7.2 Room-temperature $H_2{}^{17}O$ exchange. Pugh *et al.* showed zeolite frameworks exchange with liquid $H_2{}^{17}O$ at ambient temperature, a paradigm now adapted for other oxides and suggests opportunities for POM salts/hosts where lattice O is labile.[43,167]

7.3 Mechanochemical ^{17}O labelling. Ball-milling routes can enrich carbonates and other precursors rapidly and inexpensively, enabling downstream synthesis or ion-exchange into POM matrices without high-temperature processing.[168,169]

7.4 Targeted oxide labelling for interfaces. Plasma- or vapour-assisted protocols directly label metal-oxide supports (*e.g.*, TiO_2 and silica) that interact with POMs in composites; pairing with DNP reveals atomic-level pathways of label incorporation.[93,166,167]

7.5 Survey of options. Recent reports consolidate bulk *vs.* surface strategies ($H_2{}^{17}O$, $^{17}O_2$, mechanochemistry, ALD-assisted) and decision trees for battery/oxide materials – many transferable to POM solids and POM–oxide hybrids.[19,20,166]

Notably, DNP at natural abundance can sometimes obviate labelling for solids or surfaces, providing fast ^{17}O detection (minutes) at moderate fields. Hybrid "label-light + DNP" strategies are particularly attractive for scarce POM samples or low-loading catalysts.[51]

7.2 Sensitivity and resolution improvements

7.2.1 High fields and ultrafast MAS. Pushing to ≥28–35.2 T contracts second-order quadrupolar broadening and boosts sensitivity. Hung *et al.* demonstrated residue-specific ^{17}O at 35.2 T with fast MAS, showcasing the dramatic benefits of field.

Ultrafast MAS (≥80–160 kHz) further narrows lines and enables ^{1}H-detected ^{17}O correlations for site-resolved assignments. Practical reports and comprehensive reviews now guide experiment setup under these conditions.[50,64]

7.2.2 Cryogenic MAS probes. MAS CryoProbes (cryogenically cooled RF circuitry) routinely deliver ∼3–10× S/N improvements without altering the sample, reducing scan times for dilute or mass-limited materials, which is highly relevant for enriched ^{17}O POMs. Reports across materials/biomolecular systems quantify gains and demonstrate robust multidimensional experiments using 3.2–4 mm MAS CryoProbes.[170,171]

7.2.3 Dynamic nuclear polarisation (DNP). For many solids and supported POMs, DNP remains the most powerful general-purpose boost.[172,173] Natural-abundance ^{17}O spectra of oxides can be acquired in minutes; modern primers summarize indirect (^{1}H → ^{17}O) and direct polarisation pathways and highlight practicalities (radicals, temperature, field). These advances are in line with POM studies where oxygen sites at interfaces or low coverage are otherwise invisible.[51]

7.2.4 Toward operando ^{17}O. Designing *in situ/operando* cells that preserve MAS stability, catalyst bed integrity, and gas/liquid delivery is still challenging. Cross-disciplinary roadmaps from the catalysis community emphasise synchronized multi-probe experiments, realistic feed/temperature control, and rapid-acquisition methods. These guidelines are directly applicable to POM oxidation or electrocatalysis. Selected case studies already combine ^{17}O ssNMR with DFT to investigate active oxygen species in working catalysts.[88,148,151,174]

7.3 Emerging areas

7.3.1 Bioinorganic/biomolecular hybrids. POM–biomolecule conjugates (peptides, proteins) are gaining traction as enzyme inhibitors, imaging agents, or functional hybrids. Reviews and perspectives outline binding modes, stability, and speciation challenges in biological media – an arena where ^{17}O can localize protonation and hydration at POM oxygens, map H-bond networks, and follow exchange dynamics that underlie bioactivity.[175–178]

7.3.2 Energy storage and conversion. POMs serve as redox mediators and active components in redox-flow batteries (RFBs), DSSCs, and hybrid electrodes. Recent reviews and demonstrations highlight POM-based electrolytes with multi-electron transfer and tunable potentials, including a recent demonstration of tungsten-POM RFB chemistries.[179] Here, ^{17}O NMR can distinguish lattice *vs.* peroxo/oxo species during charge–discharge, monitor O-exchange with solvent, and track structural integrity in composites. Parallel advances in ^{17}O labelling for battery oxides and in CO_2-capture materials indicate how oxygen-site data guide mechanism and durability.[67,90,180–182]

Although the high cost of enrichment, spectral congestion, and *operando* limitations still constrain routine ^{17}O NMR of POMs, rapid innovations such low-temperature or mechanochemical ^{17}O labelling, DNP-enhanced and cryogenic MAS probes, ultrahigh-field (28–35 T) and ultrafast MAS hardware are transforming sensitivity and resolution. This is opening powerful new frontiers from bioinorganic hybrids to energy-conversion systems, where oxygen-site insight drives both mechanistic understanding and materials design.

8. Conclusions and outlook

^{17}O NMR has matured into a decisive probe of oxygen chemistry in polyoxometalates, delivering site-specific insight that few techniques can match. By directly observing the nucleus that defines POM frameworks, ^{17}O spectra discriminate terminal M=O (O_t), μ-bridging (O_b/O_c), and interior (O_i) oxygens and provide quantitative fingerprints (δ_{iso}, C_Q, and η) that give detailed information on local symmetry, bonding, protonation, solvation, and counter-ion organisation. These parameters enable robust assignments across POM structures including Lindqvist, Keggin ($\alpha/\beta/\gamma$), and Dawson (α_1/α_2) families. They also provide avenues for tracking heterometal substitution (V, Nb, Ti, Ru, Sn, *etc*), and following dynamics such as $H_2{}^{17}O$ exchange and peroxo formation during oxygen-atom transfer. Multi-field and fast-MAS experimental data cleanly separate chemical-shift and quadrupolar contributions, allowing confident deconvolution of congested spectra.

The most powerful results arise when high-field magnets (≥28–35 T) and ultrafast MAS (≥80–160 kHz) are paired with targeted ^{17}O labelling (including surface-selective enrichment) and computational techniques such as DFT/GIAO for clusters and GIPAW for periodic models. These, coupled with emerging ML/AI proxy models provide a sound platform for rapid, probabilistic prediction of $\delta/C_Q/\eta$. In this integrated approach, experiment and theory complement one another, elevating ^{17}O from a "silent" framework atom to a rigorous probe of structure–function and mechanism.

Despite these advances, several constraints remain: the low natural abundance of ^{17}O and the cost of isotopic enrichment; intrinsically low sensitivity and quadrupolar broadening ($I = 5/2$); limited access to very high magnetic fields and MAS CryoProbe hardware; sequence complexity and long acquisition times (especially for dilute or paramagnetic samples); labelling selectivity/back-exchange at reactive oxygens; and modelling uncertainties (*e.g.*, functional/basis-set dependence for EFGs and shifts). Addressing these challenges requires forward-looking actions to broaden the impact and accessibility of ^{17}O NMR in POM chemistry, including:

8.1 Affordable, sustainable enrichment

Scaling room-temperature/mechanochemical ^{17}O-labelling and implementing $H_2{}^{17}O$ recovery/recycling, coupled with natural-abundance/DNP and MAS CryoProbes to reduce sample mass and acquisition time. These measures directly address the principal barriers of cost and sensitivity, thereby broadening access to ^{17}O studies and enabling larger, statistically robust investigations.

8.2 *Operando* discovery

Deploying liquid/gas-delivery MAS hardware and rapid-acquisition schemes to monitor protonation, $H_2{}^{17}O$ exchange, lattice–surface oxygen exchange, and peroxo intermediates under catalytic, electrochemical, and photochemical conditions. Capturing oxygen

speciation under working conditions establishes direct structure–function links that are not accessible *ex situ*.

8.3 Paramagnetic POMs

Extending ^{17}O NMR to paramagnetic and mixed-valent systems using very high magnetic fields, tailored pulse sequences, and tensor-aware modelling to manage line broadening and extract redox-linked oxygen metrics. Bringing catalytically relevant paramagnets into routine scope opens a key, currently under-characterised domain of POM reactivity.

8.4 Interfaces and devices

Mapping interfacial oxygens in POM–oxide, POM–carbon, and bioinorganic hybrids, and following their *operando* evolution in flow batteries, electrolyzers, and photocatalysts. Because performance bottlenecks often originate at interfaces, site-specific oxygen information is pivotal for optimising stability, charge transfer, and turnover.

8.5 Data and standards

Institutionalizing reporting of δ_{iso}, C_Q, η (with uncertainties), field/MAS dependencies, referencing protocols, and raw data with linked structural/computational inputs; promoting open benchmark libraries spanning major POM archetypes to accelerate DFT/AI. Standardized, shareable datasets enhance reproducibility, enable rapid model validation, and ensure comparability across laboratories and platforms.

With converging advances in labelling chemistry, high-field hardware, pulse design, and DFT/AI, ^{17}O NMR is poised to shift from post-hoc characterisation to real-time, *operando* mechanistic discovery across catalysis, bioinorganic chemistry, paramagnetic POMs, and sustainable energy systems.

Author contributions

Thompson Izuagie conceived and designed the study; acquired, analysed, and interpreted all data used in the composing the manuscript. In addition, he drafted the entire manuscript, critically revised all sections for important intellectual content, provided final approval of the version to be published, and agreed to be accountable for all aspects of the work. Daniel Lebbie contributed to the conceptual design of the study; participated in data acquisition, including supplying the crystallographic information file (CIF) materials used to generate Fig. 1 and other supporting literature. He critically reviewed Sections 2 and 3 of the manuscript for intellectual content, proofread the entire manuscript, approved the final version to be published, and agreed to be accountable for the accuracy and integrity of the portions to which he contributed.

Conflicts of interest

There are no conflicts to declare.

Abbreviations

AI	Artificial intelligence
B_0	Static external magnetic field strength in NMR experiments
CE/OE	Cross effect/Overhauser effect
CP	Cross polarisation
CQMAS	Constant-time quadrupolar multiple-quantum magic-angle spinning
D-RINEPT	Dipolar-refocused insensitive nuclei enhanced by polarization transfer
EDS/EELS	Energy-dispersive X-ray/Electron energy-loss spectroscopy
EPR	Electron paramagnetic resonance
EXAFS/XANES	Extended X-ray absorption fine structure/X-ray absorption near-edge structure
EXSY	Exchange spectroscopy
FFT	Fast fourier transform
GHz	Gigahertz (10^9 Hz)
HMQC	Heteronuclear multiple-quantum coherence (2D correlation experiment)
HTS	High-temperature superconductor
Ln(III)	Lanthanide(III) ions
LTS	Low-temperature superconductor
MS	Mass spectrometry
NHMFL	National high magnetic field laboratory
NMR	Nuclear magnetic resonance
OER	Oxygen evolution reaction
PDF	Pair distribution function (total-scattering analysis)
Ph	Negative base-10 logarithm of the hydrogen ion activity
POM	Polyoxometalate
POM–MOF	Polyoxometalate–metal–organic framework composite
PXRD	Powder X-ray diffraction
REAPDOR/REDOR	Rotational echo adiabatic passage double resonance/Rotational-echo double resonance
SCH	Series-connected hybrid magnet
SCXRD	Single-crystal X-ray diffraction
SEM/TEM/STEM	Scanning/Transmission/Scanning-transmission electron microscopy
T	Tesla
TEDOR	Transferred-echo double resonance
UFF	Universal force field
XAS	X-ray absorption spectroscopy
XRD	X-ray diffraction
α_1/α_2	Dawson isomer types

Data availability

No primary research results, software or code have been included and no new data were generated or analysed as part of this review.

Acknowledgements

The authors greatly acknowledge John R. Errington and Walter G. Klemperer for their tutelage on ^{17}O NMR in POM chemistry. TI is also thankful to Newcastle University, UK for research collaboration visit in 2024, the Royal Society of Chemistry for Research Fund (R227351827431) and Researcher Collaboration Grant (C235262996150). The Cambridge Crystallographic Data Centre (CCDC) is equally appreciated for License granted to the National Open University of Nigeria that helped in accessing some materials used in this review.

Notes and references

1 J. Breibeck, N. I. Gumerova and A. Rompel, *ACS Org. Inorg. Au*, 2022, **2**, 477–495.
2 Y. Zhang, Y. Li, H. Guo, Y. Guo and R. Song, *Mater. Chem. Front.*, 2024, **8**, 732–768.
3 K. Dashtian, S. Shahsavarifar, M. Usman, Y. Joseph, M. R. Ganjali, Z. Yin and M. Rahimi-Nasrabadi, *Coord. Chem. Rev.*, 2024, **504**, 215644.
4 T. Ma, R. Yan, X. Wu, M. Wang, B. Yin, S. Li, C. Cheng and A. Thomas, *Adv. Mater.*, 2024, **36**, 2310283.
5 S. Roy, D. C. Crans and T. N. Parac-Vogt, *Front. Chem.*, 2019, **7**, 646.
6 M. Samaniyan, M. Mirzaei, R. Khajavian, H. Eshtiagh-Hosseini and C. Streb, *ACS Catal.*, 2019, **9**, 10174–10191.
7 A. Haruna, Z. U. Zango, G. Tanimu, T. Izuagie, S. G. Musa, Z. N. Garba and Z. M. A. Merican, *J. Environ. Chem. Eng.*, 2024, **12**, 113542.
8 M. Laurans, K. Trinh, K. Dalla Francesca, G. Izzet, S. Alves, E. Derat, V. Humblot, O. Pluchery, D. Vuillaume, S. Lenfant, F. Volatron and A. Proust, *ACS Appl. Mater. Interfaces*, 2020, **12**, 48109–48123.
9 A. S. Cherevan, S. P. Nandan, I. Roger, R. Liu, C. Streb and D. Eder, *Adv. Sci.*, 2020, **7**, 201903511.
10 N. I. Gumerova and A. Rompel, *Chem. Soc. Rev.*, 2020, **49**, 7568–7601.
11 M. Filowitz, R. K. C. Ho, W. G. Klemperer and W. Shum, *Inorg. Chem.*, 1979, **18**, 93–103.
12 C. J. Besecker, W. G. Klemperer, D. J. Maltbie and D. A. Wright, *Inorg. Chem.*, 1985, **24**, 1027–1032.
13 M. Pascual-Borràs, X. López, A. Rodríguez-Fortea, R. J. Errington and J. M. Poblet, *Chem. Sci.*, 2014, **5**, 2031.
14 C. A. Ohlin and W. H. Casey, in *Water in Mineral Processing*, J. Drelich, Society for Mining, Metallurgy, and Exploration, Littleton, CO, 2018, pp. 187–248.
15 R. Sharma, J. Zhang and C. A. Ohlin, *Phys. Chem. Chem. Phys.*, 2016, **18**, 8235–8241.
16 K. Yamada, in *Nuclear Magnetic Resonance of Quadrupolar Nuclei in Solid Materials*, R. K. Harris and R. E. Wasylishen, John Wiley & Sons, Chichester, 2010, pp. 115–158.
17 S. E. Ashbrook and M. E. Smith, *Chem. Soc. Rev.*, 2006, **35**, 718–735.
18 I. P. Gerothanassis, *Prog. Nucl. Magn. Reson. Spectrosc.*, 2010, **56**, 95–197.
19 S. E. Ashbrook, Z. H. Davis, R. E. Morris and C. M. Rice, *Chem. Sci.*, 2021, **12**, 5016–5036.
20 X. Xia, L. Zhu, W. Tang, L. Peng and J. Chen, *Magn. Reson. Lett.*, 2024, **4**, 200120.
21 G. Wu, *Prog. Nucl. Magn. Reson. Spectrosc.*, 2019, **114–115**, 135–191.
22 A. Abragam, *The Principles of Nuclear Magnetism*, Clarendon Press, Oxford, 1983.
23 K. J. D. MacKenzie and M. E. Smith, *Multinuclear Solid-State NMR of Inorganic Materials*, Pergamon, 2002.
24 M. J. Duer, *Solid-State NMR Spectroscopy: Principles and Applications*, Blackwell Science, Oxford, 2002.
25 S. E. Ashbrook and S. Wimperis, *Prog. Nucl. Magn. Reson. Spectrosc.*, 2004, **45**, 53–108.
26 B. Reif, S. E. Ashbrook, L. Emsley and M. Hong, *Nat. Rev. Methods Primers*, 2021, **1**, 2.
27 K. Chen, *Int. J. Mol. Sci.*, 2020, **21**, 5666.
28 D. L. Bryce, *Annu. Rep. NMR Spectrosc.*, 2022, **108**, 1–46.
29 C. P. Slichter, *Principles of Magnetic Resonance*, Springer, Berlin, 1990, vol. 1.
30 J.-P. Amoureux, C. Fernandez and S. Steuernagel, *J. Magn. Reson. A*, 1996, **123**, 116–118.
31 A. J. Vega, in *Encyclopedia of Magnetic Resonance*, John Wiley & Sons, Chichester, 2010.
32 E. G. Keeler, V. K. Michaelis, M. T. Colvin, I. Hung, P. L. Gor'kov, T. A. Cross, Z. Gan and R. G. Griffin, *J. Am. Chem. Soc.*, 2017, **139**, 17953–17963.
33 J. Shen, V. Terskikh, J. Struppe, A. Hassan, M. Monette, I. Hung, Z. Gan, A. Brinkmann and G. Wu, *Chem. Sci.*, 2022, **13**, 2591–2603.
34 J. Špačková, C. Fabra, G. Cazals, M. Hubert-Roux, I. Schmitz-Afonso, I. Goldberga, D. Berthomieu, A. Lebrun, T.-X. Métro and D. Laurencin, *Chem. Commun.*, 2021, **57**, 6812–6815.
35 I. Goldberga, N. Patris, C.-H. Chen, E. Thomassot, J. Trébosc, I. Hung, Z. Gan, D. Berthomieu, T.-X. Métro, C. Bonhomme, C. Gervais and D. Laurencin, *J. Phys. Chem. C*, 2022, **126**, 12044–12059.
36 D. Lebbie, T. Izuagie, M. Pascual-Borràs, B. Kandasamy, C. Wills, P. G. Waddell, B. R. Horrocks and R. J. Errington, *Inorg. Chem.*, 2025, **64**, 2379–2393.
37 T. Izuagie, *Synthesis of Polyoxometalates for Detailed Solution Reactivity Studies*, PhD thesis, Newcastle University, 2017.
38 R. J. Errington, S. S. Petkar, P. S. Middleton, W. McFarlane, W. Clegg, R. A. Coxall and R. W. Harrington, *Dalton Trans.*, 2007, **44**, 5211–5222.
39 R. J. Errington, in *Polyoxometalate Chemistry*, R. van Eldik and L. Cronin, Academic Press, Amsterdam, 2017, pp. 287–336.
40 R. J. Errington, S. S. Petkar, P. S. Middleton, W. McFarlane, W. Clegg, R. A. Coxall and R. W. Harrington, *J. Am. Chem. Soc.*, 2007, **129**, 12181–12196.
41 J. R. Black, M. Nyman and W. H. Casey, *J. Am. Chem. Soc.*, 2006, **128**, 14712–14720.
42 K. Chen, A. Zornes, V. Nguyen, B. Wang, Z. Gan, S. P. Crossley and J. L. White, *J. Am. Chem. Soc.*, 2022, **144**, 16916–16929.

43 S. M. Pugh, P. A. Wright, D. J. Law, N. Thompson and S. E. Ashbrook, *J. Am. Chem. Soc.*, 2020, **142**, 900–906.
44 N. I. Gumerova and A. Rompel, *Sci. Adv.*, 2024, **9**, 0814.
45 J. Špačková, I. Goldberga, R. Yadav, G. Cazals, A. Lebrun, P. Verdié, T. Métro and D. Laurencin, *Chem.–Eur. J.*, 2022, **29**, e202203014.
46 E. N. Bassey, P. J. Reeves, I. D. Seymour and C. P. Grey, *J. Am. Chem. Soc.*, 2022, **144**, 18714–18729.
47 N. J. Brownbill, D. Gajan, A. Lesage, L. Emsley and F. Blanc, *Chem. Commun.*, 2017, **53**, 2563–2566.
48 T. Polenova, R. Gupta and A. Goldbourt, *Anal. Chem.*, 2015, **87**, 5458–5469.
49 P.-H. Chien, K. J. Griffith, H. Liu, Z. Gan and Y.-Y. Hu, *Annu. Rev. Mater. Res.*, 2020, **50**, 493–520.
50 I. Hung, E. G. Keeler, W. Mao, P. L. Gor'kov, R. G. Griffin and Z. Gan, *J. Phys. Chem. Lett.*, 2022, **13**, 6549–6558.
51 F. Blanc, L. Sperrin, D. A. Jefferson, S. Pawsey, M. Rosay and C. P. Grey, *J. Am. Chem. Soc.*, 2013, **135**, 2975–2978.
52 A. J. Rossini, A. Zagdoun, M. Lelli, A. Lesage, C. Copéret and L. Emsley, *Acc. Chem. Res.*, 2013, **46**, 1942–1951.
53 R. W. Hooper, B. A. Klein and V. K. Michaelis, *Chem. Mater.*, 2020, **32**, 4425–4430.
54 K. Nishimura, H. Kouno, Y. Kawashima, K. Orihashi, S. Fujiwara, K. Tateishi, T. Uesaka, N. Kimizuka and N. Yanai, *Chem. Commun.*, 2020, **56**, 7217–7232.
55 T. Hamachi and N. Yanai, *Prog. Nucl. Magn. Reson. Spectrosc.*, 2024, **142–143**, 55–68.
56 J. T. Arnold, S. S. Dharmatti and M. E. Packard, *J. Chem. Phys.*, 1951, **19**, 507.
57 W. G. Klemperer, *Angew. Chem., Int. Ed.*, 1978, **17**, 246–254.
58 M. Filowitz, W. G. Klemperer, L. Messerle and W. Shum, *J. Am. Chem. Soc.*, 1976, **98**, 2345–2346.
59 G. L. Turner, S. E. Chung and E. Oldfield, *J. Magn. Reson.*, 1985, **64**, 316–324.
60 L. Frydman and J. S. Harwood, *J. Am. Chem. Soc.*, 1995, **117**, 5367–5368.
61 Z. Gan, *J. Am. Chem. Soc.*, 2000, **122**, 3242–3243.
62 C. J. Pickard and F. Mauri, *Phys. Rev. B: Condens. Matter Mater. Phys.*, 2001, **63**, 245101.
63 J. R. Yates, C. J. Pickard and F. Mauri, *Phys. Rev. B: Condens. Matter Mater. Phys.*, 2007, **76**, 024401.
64 Y. Nishiyama, G. Hou, V. Agarwal, Y. Su and A. Ramamoorthy, *Chem. Rev.*, 2023, **123**, 918–988.
65 D. Jardón-Álvarez, G. Reuveni, A. Harchol and M. Leskes, *J. Phys. Chem. Lett.*, 2020, **11**, 5439–5445.
66 Z. Gan, I. Hung, X. Wang, J. Paulino, G. Wu, I. M. Litvak, P. L. Gor'kov, W. W. Brey, P. Lendi, J. L. Schiano, M. D. Bird, I. R. Dixon, J. Toth, G. S. Boebinger and T. A. Cross, *J. Magn. Reson.*, 2017, **284**, 125–136.
67 Y. Wen, W. Zhang, J. Wen, F. Wang, X. Ke, J. Chen and L. Peng, *J. Phys. Chem. Lett.*, 2024, **15**, 11587–11592.
68 B. Song, Y. Li, Y. Sun, L. Peng and L.-H. Xie, *Phys. Chem. Chem. Phys.*, 2024, **26**, 7890–7895.
69 I. Goldberga, I. Hung, V. Sarou-Kanian, C. Gervais, Z. Gan, J. Novák-Špačková, T.-X. Métro, C. Leroy, D. Berthomieu, A. van der Lee, C. Bonhomme and D. Laurencin, *Inorg. Chem.*, 2024, **63**, 10179–10193.
70 Y. Wen, F. Wang, H. Zhu, C. Yang, X. Ke, W. Li, H. Huo and L. Peng, *ACS Omega*, 2025, **10**, 13655–13663.
71 W. Wang, J. Xu and F. Deng, *Natl. Sci. Rev.*, 2024, **9**, nwac155.
72 D. S. Wishart, *J. Magn. Reson.*, 2019, **306**, 155–161.
73 E. Moser, E. Laistler, F. Schmitt and G. Kontaxis, *Front. Phys.*, 2017, **5**, 00033.
74 V. Martins, J. Xu, I. Hung, Z. Gan, C. Gervais, C. Bonhomme and Y. Huang, *Magn. Reson. Chem.*, 2021, **59**, 940–950.
75 I. Hung, Z. Gan and G. Wu, *J. Phys. Chem. Lett.*, 2021, **12**, 8897–8902.
76 Z. J. Berkson, S. Björgvinsdóttir, A. Yakimov, D. Gioffrè, M. D. Korzyński, A. B. Barnes and C. Copéret, *JACS Au*, 2022, **2**, 2460–2465.
77 R. W. Dorn, A. L. Paterson, I. Hung, P. L. Gor'kov, A. J. Thompson, A. D. Sadow, Z. Gan and A. J. Rossini, *J. Phys. Chem. C*, 2022, **126**, 11652–11666.
78 T. Gopinath, K. Shin, Y. Tian, W. Im, J. Struppe, B. Perrone, A. Hassan and F. M. Marassi, *J. Struct. Biol.*, 2024, **216**, 108061.
79 R. W. Dorn, L. O. Mark, I. Hung, M. C. Cendejas, Y. Xu, P. L. Gor'kov, W. Mao, F. Ibrahim, Z. Gan, I. Hermans and A. J. Rossini, *J. Am. Chem. Soc.*, 2022, **144**, 18766–18771.
80 D. Carnevale, G. Mouchaham, S. Wang, M. Baudin, C. Serre, G. Bodenhausen and D. Abergel, *Phys. Chem. Chem. Phys.*, 2021, **23**, 2245–2251.
81 M. A. Hope, D. M. Halat, P. C. M. M. Magusin, S. Paul, L. Peng and C. P. Grey, *Chem. Commun.*, 2017, **53**, 2142–2145.
82 F. A. Perras, Z. Wang, P. Naik, I. I. Slowing and M. Pruski, *Angew. Chem., Int. Ed.*, 2017, **56**, 9165–9169.
83 V. K. Michaelis, E. G. Keeler, S. Bahri, T.-C. Ong, E. Daviso, M. T. Colvin and R. G. Griffin, *J. Phys. Chem. B*, 2022, **126**, 7847–7856.
84 G. Menzildjian, J. Schlagnitweit, G. Casano, O. Ouari, D. Gajan and A. Lesage, *Chem. Sci.*, 2023, **14**, 6120–6148.
85 L. Niccoli, G. Casano, G. Menzildjian, M. Yulikov, T. Robinson, S.-E. Akrial, Z. Wang, C. Reiter, A. Purea, D. Siri, A. Venkatesh, L. Emsley, D. Gajan, M. Lelli, O. Ouari and A. Lesage, *Chem. Sci.*, 2024, **15**, 16582–16593.
86 D. Jardón-Álvarez and M. Leskes, *Prog. Nucl. Magn. Reson. Spectrosc.*, 2023, **138–139**, 70–104.
87 C. Leroy, T.-X. Métro, I. Hung, Z. Gan, C. Gervais and D. Laurencin, *Chem. Mater.*, 2022, **34**, 2292–2312.
88 B. Roldán Cuenya and M. A. Bañares, *Chem. Rev.*, 2024, **124**, 8011–8013.
89 O. M. Magnussen, J. Drnec, C. Qiu, I. Martens, J. J. Huang, R. Chattot and A. Singer, *Chem. Rev.*, 2024, **124**, 629–721.
90 A. H. Berge, S. M. Pugh, M. I. M. Short, C. Kaur, Z. Lu, J.-H. Lee, C. J. Pickard, A. Sayari and A. C. Forse, *Nat. Commun.*, 2022, **13**, 7763.
91 Z. Zhu, R. Luo and E. W. Zhao, *Magn. Reson. Lett.*, 2024, **4**, 100096.
92 M. E. Smith, *Phys. Chem. Chem. Phys.*, 2023, **25**, 26–47.
93 C.-H. Chen, E. Gaillard, F. Mentink-Vigier, K. Chen, Z. Gan, P. Gaveau, B. Rebière, R. Berthelot, P. Florian,

C. Bonhomme, M. E. Smith, T.-X. Métro, B. Alonso and D. Laurencin, *Inorg. Chem.*, 2020, **59**, 13050–13066.
94 F. A. Perras, T. Kobayashi and M. Pruski, *J. Am. Chem. Soc.*, 2015, **137**, 8336–8339.
95 A. J. Rossini, *J. Phys. Chem. Lett.*, 2018, **9**, 5150–5159.
96 T. Charpentier, *Solid State Nucl. Magn. Reson.*, 2011, **40**, 1–20.
97 C. Tantardini, A. G. Kvashnin and D. Ceresoli, *Materials*, 2022, **15**, 3347.
98 R. P. Martinho and L. Frydman, *Chem.–Eur. J.*, 2022, e202201490.
99 I. Cortés, C. Cuadrado, A. Hernández Daranas and A. M. Sarotti, *Front. Nat. Prod.*, 2023, 1122426.
100 K. T. Mueller, Y. Wu, B. F. Chmelka, J. Stebbins and A. Pines, *J. Am. Chem. Soc.*, 1991, **113**, 32–38.
101 T. J. Bastow, A. F. Moodie, M. E. Smith and H. J. Whitfield, *J. Mater. Chem.*, 1993, **3**, 697–702.
102 J. Gracia, J. M. Poblet, J. Autschbach and L. P. Kazansky, *Eur. J. Inorg. Chem.*, 2006, **2006**, 1139–1148.
103 D. Lebbie, *Non-aqueous Protonation, Protonolysis and Related Reactions of Polyoxometalates*, PhD thesis, Newcastle University, 2020.
104 D. Nowicka, N. Vadra, E. Wieczorek-Szweda, V. Patroniak and A. Gorczyński, *Coord. Chem. Rev.*, 2024, **519**, 216091.
105 W. G. Klemperer and K. A. Marek, *Eur. J. Inorg. Chem.*, 2013, **2013**, 1762–1771.
106 L. Coyle, P. S. Middleton, C. J. Murphy, W. Clegg, R. W. Harrington and R. J. Errington, *Dalton Trans.*, 2012, **41**, 971–981.
107 R. I. Maksimovskaya and M. A. Fedotov, *J. Struct. Chem.*, 1981, **22**, 129–131.
108 M. Pascual-Borràs, X. López and J. M. Poblet, *Phys. Chem. Chem. Phys.*, 2015, **17**, 8723–8731.
109 T. Ueda, Y. Nishimoto, R. Saito, M. Ohnishi and J. Nambu, *Inorganics*, 2015, **3**, 355–369.
110 B. Kandasamy, C. Wills, W. McFarlane, W. Clegg, R. W. Harrington, A. Rodríguez-Fortea, J. M. Poblet, P. G. Bruce and R. J. Errington, *Chem.–Eur. J.*, 2012, **18**, 59–62.
111 M. Inoue, T. Yamase and L. P. Kazansky, *Polyhedron*, 2003, **22**, 1183–1189.
112 R. I. Maksimovskaya and K. G. Burtseva, *Polyhedron*, 1985, **4**, 1559–1562.
113 C. Boglio, B. Hasenknopf, G. Lenoble, P. Rémy, P. Gouzerh, S. Thorimbert, E. Lacôte, M. Malacria and R. Thouvenot, *Chem.–Eur. J.*, 2008, **14**, 1532–1540.
114 J. M. Cameron, L. Vilà-Nadal, R. S. Winter, F. Iijima, J. C. Murillo, A. Rodríguez-Fortea, H. Oshio, J. M. Poblet and L. Cronin, *J. Am. Chem. Soc.*, 2016, **138**, 8765–8773.
115 R. I. Maksimovskaya and N. N. Chumachenko, *Polyhedron*, 1987, **6**, 1813–1821.
116 Y. Martinetto, B. Pégot, C. Roch-Marchal, M. Haouas, B. Cottyn-Boitte, F. Camerel, J. Jeftic, D. Morineau, E. Magnier and S. Floquet, *New J. Chem.*, 2021, **45**, 9751–9755.
117 L. P. Kazansky, P. Chaquin, M. Fournier and G. Hervé, *Polyhedron*, 1998, **17**, 4353–4364.
118 L. P. Kazansky and B. R. McGarvey, *Coord. Chem. Rev.*, 1999, **188**, 157–210.
119 S. Muniyappan, Y. Lin, Y.-H. Lee and J. H. Kim, *Biology*, 2021, **10**, 453.
120 R. van Eldik and L. Cronin, *Polyoxometalate Chemistry*, Academic Press, 2017.
121 Y. Ji, K. Chen, X. Han, X. Bao and G. Hou, *J. Am. Chem. Soc.*, 2024, **146**, 11211–11224.
122 C. Ehinger, C. P. Gordon and C. Copéret, *Chem. Sci.*, 2019, **10**, 1786–1795.
123 O. W. Howarth, *Dalton Trans.*, 2004, **3**, 476.
124 X. López, J. J. Carbó, C. Bo and J. M. Poblet, *Chem. Soc. Rev.*, 2012, **41**, 7537–7571.
125 S. L. Carnahan, B. J. Lampkin, P. Naik, M. P. Hanrahan, I. I. Slowing, B. VanVeller, G. Wu and A. J. Rossini, *J. Am. Chem. Soc.*, 2019, **141**, 441–450.
126 M. T. Pope and A. Müller, *Angew Chem. Int. Ed. Engl.*, 1991, **30**, 34–48.
127 L.-X. Cai, Y.-H. Hu, L.-P. Zhou, P.-M. Cheng, X.-Q. Guo, Y.-T. Chan and Q.-F. Sun, *Chem. Sci.*, 2025, **16**, 7956–7962.
128 E. G. Keeler, V. K. Michaelis, C. B. Wilson, I. Hung, X. Wang, Z. Gan and R. G. Griffin, *J. Phys. Chem. B*, 2019, **123**, 3061–3067.
129 A. Wong, A. P. Howes, J. R. Yates, A. Watts, T. Anupõld, J. Past, A. Samoson, R. Dupree and M. E. Smith, *Phys. Chem. Chem. Phys.*, 2011, **13**, 12213–12224.
130 M. A. Fedotov, R. I. Maksimovskaya, D. U. Begalieva and A. K. Il'yasova, *Bull. Acad. Sci. USSR Div. Chem. Sci.*, 1980, **29**, 1025–1028.
131 D. Gao, I. Trentin, L. Schwiedrzik, L. González and C. Streb, *Molecules*, 2019, **25**, 157.
132 Y. Ji, K. Chen, A. Hao and G. Hou, *J. Magn. Reson. Open*, 2025, **22**, 100182.
133 V. W. Day and W. G. Klemperer, *Science*, 1985, **228**, 533–541.
134 L. Pettersson, I. Andersson, F. Taube, I. Toth, M. Hashimoto and O. W. Howarth, *Dalton Trans.*, 2003, **32**, 146–152.
135 E. Schreiber, A. A. Fertig, W. W. Brennessel and E. M. Matson, *J. Am. Chem. Soc.*, 2022, **144**, 5029–5041.
136 B. E. Petel, W. W. Brennessel and E. M. Matson, *J. Am. Chem. Soc.*, 2018, **140**, 8424–8428.
137 E. Schreiber, W. W. Brennessel and E. M. Matson, *Chem. Sci.*, 2023, **14**, 1386–1396.
138 B. E. Petel and E. M. Matson, *Chem. Commun.*, 2020, **56**, 13477–13490.
139 B. B. Sarma and R. Neumann, *Nat. Commun.*, 2014, **5**, 4621.
140 A. T. Harrison and O. W. Howarth, *J. Chem. Soc., Dalton Trans.*, 1985, **14**, 1953–1957.
141 W. Hu, N. R. Jaegers, A. D. Winkelman, S. Murali, K. T. Mueller, Y. Wang and J. Z. Hu, *Front. Catal.*, 2022, **2**, 935174.
142 V. K. Velisoju, S. R. Kulkarni, M. Cui, A. I. M. Rabee, P. Paalanen, J. Rabeah, M. Maestri, A. Brückner, J. Ruiz-Martinez and P. Castaño, *Chem Catal.*, 2023, **3**, 100666.

143 B. B. Xu, Y. Liu, Y. Liu, X. You, H. Zhou, Y. N. Xu, P. F. Liu, H. F. Wang, H. G. Yang, X. L. Wang and Y. F. Yao, *Chem*, 2024, **10**, 3114–3130.
144 L. Chen, X. Ding, Z. Wang, S. Xu, Q. Jiang, C. Dun and J. J. Urban, *Surf. Sci. Technol.*, 2024, **2**, 9.
145 E. M. Villa, C. A. Ohlin and W. H. Casey, *Am. J. Sci.*, 2010, **310**, 629–644.
146 S. Jovanovic, P. P. M. Schleker, M. Streun, S. Merz, P. Jakes, M. Schatz, R.-A. Eichel and J. Granwehr, *Magn. Reson.*, 2021, **2**, 265–280.
147 R. Dervişoğlu, D. S. Middlemiss, F. Blanc, Y.-L. Lee, D. Morgan and C. P. Grey, *Chem. Mater.*, 2015, **27**, 3861–3873.
148 N. R. Jaegers, K. T. Mueller, Y. Wang and J. Z. Hu, *Acc. Chem. Res.*, 2020, **53**, 611–619.
149 Y. Li, X.-P. Wu, N. Jiang, M. Lin, L. Shen, H. Sun, Y. Wang, M. Wang, X. Ke, Z. Yu, F. Gao, L. Dong, X. Guo, W. Hou, W. Ding, X.-Q. Gong, C. P. Grey and L. Peng, *Nat. Commun.*, 2017, **8**, 581.
150 N. Feng, J. Xu and F. Deng, *Chem. Synth.*, 2024, **4**, 43.
151 Y. Wen, F. Wang, J. Zhu, Q. Wen, X. Xia, J. Wen, C. Deng, J.-H. Du, X. Ke, Z. Zhang, H. Guan, L. Nie, M. Wang, W. Hou, W. Li, W. Tang, W. Ding, J. Chen and L. Peng, *Nat. Commun.*, 2025, **16**, 3537.
152 J. Vícha, J. Novotný, S. Komorovský, M. Straka, M. Kaupp and R. Marek, *Chem. Rev.*, 2020, **120**, 7065–7103.
153 J. V. Reina, F. Civaia, A. F. Harper, C. Scheurer and S. S. Köcher, *Faraday Discuss.*, 2025, **255**, 266–287.
154 H. Sun, S. Dwaraknath, H. Ling, X. Qu, P. Huck, K. A. Persson and S. E. Hayes, *NPJ Comput. Mater.*, 2020, **6**, 53.
155 J. D. Hartman, A. Mathews and J. K. Harper, *Front. Chem.*, 2021, **9**, 751711.
156 A. Marchenko, L. A. Truflandier and J. Autschbach, *Inorg. Chem.*, 2017, **56**, 7384–7396.
157 F. M. Paruzzo, A. Hofstetter, F. Musil, S. De, M. Ceriotti and L. Emsley, *Nat. Commun.*, 2018, **9**, 4501.
158 H. Sun, S. Dwaraknath, H. Ling, K. A. Persson and S. E. Hayes, *Sci. Rep.*, 2025, **15**, 26456.
159 M. Cordova, E. A. Engel, A. Stefaniuk, F. Paruzzo, A. Hofstetter, M. Ceriotti and L. Emsley, *J. Phys. Chem. C*, 2022, **126**, 16710–16720.
160 M. C. Venetos, M. Wen and K. A. Persson, *J. Phys. Chem. A*, 2023, **127**, 2388–2398.
161 C. Ben Mahmoud, L. A. M. Rosset, J. R. Yates and V. L. Deringer, *J. Chem. Phys.*, 2024, **160**, 174801.
162 C. Han, D. Zhang, S. Xia and Y. Zhang, *J. Chem. Theory Comput.*, 2024, **20**, 5250–5258.
163 M. Bertani, A. Pedone, F. Faglioni and T. Charpentier, *ChemPhysChem*, 2023, **24**, e202300782.
164 Y. Luo, W. Chen, Z. Su, X. Shi, J. Luo, X. Qu, Z. Chen and Y. Lin, *Nat. Commun.*, 2025, **16**, 2342.
165 F. De Lorenzi, T. Weinmann, S. Bruderer, B. Heitmann, A. Henrici and S. Stingelin, *J. Magn. Reson.*, 2024, **364**, 107723.
166 J. Chen, X. Liu, L. Shen, K. Chen, Y. Wen, Y. Wang, X. Xia, F. Wang, J. S. Gomez, I. Hung, W. Tang, Z. Gan, J.-H. Du, R. Chen and L. Peng, *J. Phys. Chem. Lett.*, 2025, **16**, 6907–6913.
167 A. Agarwal, M. Mais and F. A. Perras, *Chem. Commun.*, 2024, **60**, 12189–12192.
168 A. Peach, N. Fabregue, C. Erre, T.-X. Métro, D. Gajan, F. Mentink-Vigier, F. Scott, J. Trébosc, F. Voron, N. Patris, C. Gervais and D. Laurencin, *Chem. Sci.*, 2025, **16**, 10731–10741.
169 C. Chen, F. Mentink-Vigier, J. Trébosc, I. Goldberga, P. Gaveau, E. Thomassot, D. Iuga, M. E. Smith, K. Chen, Z. Gan, N. Fabregue, T. Métro, B. Alonso and D. Laurencin, *Chem.–Eur. J.*, 2021, **27**, 12574–12588.
170 A. Hassan, C. M. Quinn, J. Struppe, I. V. Sergeyev, C. Zhang, C. Guo, B. Runge, T. Theint, H. H. Dao, C. P. Jaroniec, M. Berbon, A. Lends, B. Habenstein, A. Loquet, R. Kuemmerle, B. Perrone, A. M. Gronenborn and T. Polenova, *J. Magn. Reson.*, 2020, **311**, 106680.
171 A. Vallet, I. Ayala, B. Perrone, A. Hassan, J.-P. Simorre, C. Bougault and P. Schanda, *J. Magn. Reson.*, 2024, **364**, 107708.
172 S. J. Elliott, B. B. Duff, A. R. Taylor-Hughes, D. J. Cheney, J. P. Corley, S. Paul, A. Brookfield, S. Pawsey, D. Gajan, H. C. Aspinall, A. Lesage and F. Blanc, *J. Phys. Chem. B*, 2022, **126**, 6281–6289.
173 I. B. Moroz, N. Katzav, A. Svirinovsky-Arbeli and M. Leskes, *J. Magn. Reson. Open*, 2024, **21**, 100173.
174 M. T. Suekuni, C. D'Agostino and A. M. Allgeier, *ACS Catal.*, 2025, **15**, 2063–2081.
175 N. I. Gumerova and A. Rompel, *Inorg. Chem.*, 2021, **60**, 6109–6114.
176 H. Soria-Carrera, E. Atrián-Blasco, R. Martín-Rapún and S. G. Mitchell, *Chem. Sci.*, 2023, **14**, 10–28.
177 S. Lentink, D. E. Salazar Marcano, M. A. Moussawi and T. N. Parac-Vogt, *Angew. Chem., Int. Ed.*, 2023, **62**, e202303817.
178 R. Fu and A. Ramamoorthy, *J. Phys. Chem. B*, 2024, **128**, 3527–3537.
179 L.-P. Cui, S. Zhang, Y. Zhao, X.-Y. Ge, L. Yang, K. Li, L.-B. Feng, R.-G. Li and J.-J. Chen, *Nat. Commun.*, 2025, **16**, 3674.
180 Y. Liu, J. Zhang, S. Lu and Y. Xiang, *Mater. Rep.: Energy*, 2022, **2**, 100094.
181 B. J. Rhodes, L. L. Schaaf, M. E. Zick, S. M. Pugh, J. S. Hilliard, S. Sharma, C. R. Wade, P. J. Milner, G. Csányi and A. C. Forse, *ChemPhysChem*, 2024, **26**, e202400941.
182 W. Li, W. Xu, Z. Sun, L. Tang, G. Xu, X. He, Y. Deng, W. Sun, B. Zhou, J. Song and W. Liu, *Nat. Commun.*, 2025, **16**, 4654.